T F A

ACTA FACULTATIS TECHNICAE

TECHNICAL UNIVERSITY IN ZVOLEN

2

ISSUE: XXVI
ZVOLEN 2021

Medzinárodný zbor recenzentov / International Reviewers Board

Mendel University in Brno, Faculty of Forestry and Wood Technology
Alena Očkajová (SK)
Matej Bel University, Faculty of Natural Sciences
Marián Peciar (SK)
Slovak University of Technology in Bratislava, Faculty of Mechanical Engineering
Krzysztof Zbigniew Rokosz (PL)
Koszalin University of Technology, Faculty of Mechanical Engineering
Juraj Ružbarský (SK)
Technical University of Košice, Faculty of Manufacturing Technologies
Ruslan Safin (RU)
Kazan National Research Technological University
Sergey Spiridonov (RU)
State Institution of Higher Professional Education, Saint Petersburg State
Dana Stančeková (SK)
University of Žilina,Faculty of Mechanical Engineering
Vladimír Štollmann (SK)
Technical University in Zvolen, Faculty of Forestry
Marian Šušniar (HR)
University of Zagreb, Faculty of Forestry
Paweł Tylek (PL)
University of Agriculture in Krakow, Faculty of Forestry
Valery Zhylinski (BY)
Belarusian State Technological University

TABLE OF CONTENTS

SCIENTIFIC PAPERS

REVIEW

SCIENTIFIC PAPERS

ANALYSIS OF HYDROGENATED VEGETABLE OIL INJECTION USING A HIGH-SPEED CAMERA

ANALÝZA ROSTŘIKU HYDROGENOVÉHO ROSTLINNÉHO OLEJE POMOCÍ RYCHLOKAMERY

Jaroslav Mrázek, Jakub Čedík, Martin Pexa, Michal Holubek

[1]Department for Quality and Dependability of Machines Czech University of Life Sciences Prague, Faculty of Engineering, Kamýcká 129, 165 21, Prague 6, Czech Republic, mrazekjaroslav@tf.czu.cz

Abstract: One of the biofuels that have the potential to replace fossil fuels as internal combustion engine propulsion is hydrogenated oil (HVO). Hydrogenated oil has parameters that are close to diesel, yet they are not the same. Different parameters include, for example, the viscosity and density of the fuel, which will affect the way the fuel is sprayed in the combustion chamber and thus also the operating parameters of the engine. The paper focuses on the analysis of HVO spraying at different levels of concentration (HVO_5, HVO_10 and HVO_100). For comparison, a spray of standard diesel (D100) was used as a standard. A high-speed camera was used to obtain data, and the subsequent analysis dealt with the maximum width of the sprayed cone, the spray angle, the aerosol propagation rate and its acceleration. The analysis of fuel spraying showed mainly the effect of higher viscosity of blended fuels and pure HVO, which is evidenced mainly by the lower measured width of the sprayed aerosol cone and the smaller spray angle compared to D100 fuel.

Key words: Biofuel, HVO (hydrogenated vegetable oil), Injection, High-speed camera

Abstract: Jedním z biopaliv, které mají potenciál nahradit fosilní paliva jako pohon spalovacího motoru je hydrogenovaný olej (HVO). Hydrogenovaný olej má parametry, které se blíží motorové naftě, přesto stejné nejsou. Mezi rozdílné parametry patří například viskozita a hustota paliva, která bude mít vliv na způsob rozprášení paliva ve spalovacím prostoru a tedy i na provozní parametry motoru. Příspěvek je zaměřen na analýzu rozstřiku HVO v různé úrovni koncentrace (HVO_5, HVO_10 a HVO_100). Pro porovnání bylo jako etalonu použito srozstřiku standardní motorové nafty (D100). Pro zisk dat byla použita rychlokamera a následná analýza se zabývala maximální šířkou rozstřikovaného kužele, úhlem rozstřiku, rychlostí šíření aerosolu a jeho zrychlení. Analýza nástřiku paliva ukázala hlavně účinek vyšší viskozity směsných paliv a čistého HVO, což dokládá především nižší naměřená šířka stříkaného aerosolového kužele a menší úhel rozstřiku ve srovnání s palivem D100.

Klíčová slová: Biopaliva, HVO (Hydrogenovaný rostlinný olej), Vstřik, rychlokamera

INTRODUCTION

Vegetable oils are a raw material for the production of biofuels used as alternative fuels (Bortel *et al*. 2018, Elango and Senthilkumar 2011, Esteba *et al*. 2012). In the form of biodiesel, they are the dominant biofuel used to power diesel engines (Pechout *et al*. 2019,

Sondors *et al*. 2019). Much better quality diesel fuel than conventional biodiesel can be produced from vegetable oils by their hydrogenation. In Europe, the largest producer of HVO (hydrogenated vegetable oil) is the Finnish company Neste Oil.

HVO as a possible alternative fuel for engines has shown excellent combustion and emission characteristics in many studies (Birzietis *et al*. 2017, Bohl *et al*. 2018, Bortel *et al*. 2019, Heikkilä et al. 2012, Omari *et al*. 2017). It can be produced from various sources - such as waste oil, rapeseed oil or palm oil and animal fat (Soam and Hillman 2019, Zeman et al. 2019). Vojtíšek-Lom *et al*. (2017) reported that cold starts led to an increase in the concentration of particulates and bound organic compounds in emissions of approximately 15% compared to warm starts.

This fuel can be used separately as a sulfur-free hydrocarbon, a non-aromatic fuel with a high cetane number, excellent low-temperature properties and high oxidative stability. The second option is its addition to diesel (Bohl *et al*. 2017, Dimitriadis *et al*. 2020, Hissa *et al*. 2019, Honig *et al*. 2015, Vojtíšek-Lom *et al*. 2017). HVO fuel also has a positive effect on emissions (solid particles by 33%, NOx by 9%, CO by 24% and HC by 30%), does not smell during combustion and has better ignition parameters, less smoke, and keeps the combustion chamber and nozzles clean (Cheng et al. 2019, Nordelöf *et al*. 2019, Rimkus *et al*. 2019, Zhang *et al*. 2017).

More than 60% of the raw material of waste character = 2nd generation biofuels are used for the production of HVO. Compared to biodiesel, HVO has the advantage as a fuel of its hydrocarbon nature. HVO is materially compatible with the fuel system and is characterized by good oxidative stability (Krivopolianskii *et al*. 2019, Pexa *et al*. 2014, Rodríguez-Fernández *et al*. 2017, Sunde *et al*. 2011). HVO has some better properties than diesel (sulfur content, cetane number, low aromatic hydrocarbons). HVO can be added to diesel in any amount. The relatively low HVO density reduces the density of the blended fuel (at 30% by volume of HVO in diesel, the density approaches the lower limit (EN-590)). At the same time, at 30% of the HVO content in the fuel, an increase in the cetane number of up to 10 units can be expected (Gailis *et al*. 2017, Pechout and Macoun 2019, Sondors et al. 2019, Suarez-Bertoa *et al*. 2019). Diesel fuel containing HVO can also be found in the Czech Republic (Maxxmotion Diesel - OMV).

The aim of this research was to obtain data on the spraying of HVO at different levels of concentration (HVO_5, HVO_10 and HVO_100) and then compare it with the spraying of standard diesel (D100).

MATERIAL AND METHODS

The evaluation of the spray was performed on the basis of the recording from the speed camera. Based on the experience gained during the solution of the IGA project in 2019 with a loaned Fastcam Mini AX200 camera from the company Proxis, shooting was carried out with a high-speed camera Photron Fasctam NOVA S9 (Fig. 1), borrowed from the same company. The shooting was carried out in the form of a service from the above-mentioned company. Basic parameters of selected camera are: Maximum frame rate 900 000fps, Class Leading Light Sensitivity: ISO 64,000 monochrome, ISO 16,000 color, Global Electronic Shutter: 1ms to 0.2µs independent of frame rate, Dynamic Range (ADC): 12-bit monochrome, 36-bit color. The frame rate was selected at 15,000 frames per second. In

addition to the mentioned fuel mixtures HVO_5 and HVO_10 and reference fuel D100, pure HVO (HVO_100) was also used to evaluate the influence of fuel on its spray. The measurement took place at the starting speed of the internal combustion engine, where the dismantled injector ensured that no single commissioning would take place.

The analysis of recordings from the speed camera was performed using the program Photron fastcam Viewer version 4.0.4.1. Regarding the spray itself, 4 criteria were evaluated for each fuel – the maximum width of the sprayed cone, the spray angle, aerosol spread rate and acceleration. To measure the width and angle of the spray, 10 measuring points were determined from the beginning of the injection to the end. The speed of the fuel sprayed was measured from the start of the spray to the edge of the camera so that 10 measuring points were determined again and the distance by which the aerosol changed its position for a given number of images was measured using the distance measurement function in the program. Characteristics for used fuels are in table 1.

Fig. 1 Photron Fasctam NOVA S9 camera and whole test equipment
Obr. 1 Kamera Photron Fasctam NOVA S9 a celé testovacie zariadenie

Table 1 Characteristics of used fuels 1
Tabuľka 1 Charakteristiky použitých palív

Characteristic [unit]	**Diesel**	**HVO**
Density [kg/m3] (T= 15 °C)	835,2	779,1
Viscosity [mm2/s] (T= 40 °C)	2,8	2,7
Cetane number [–]	54,18	75,5
Lubricity [µm]	386	316
Flash point [°C]	–	70
Lower heating value [MJ/kg]	39,79	43,9
Initial Boiling Point [°C]	155,1	185,5
Final Boiling Point [°C]	363,1	302
Total contamination [mg/kg]	<24	6
Carbon content [% m/m]	85,3	85,7
Hydrogen Content [% m/m]	13,4	14,3

RESULTS AND DISCUSSION

The individual sprays can be seen in Figures 2, 3, 4 and 5.

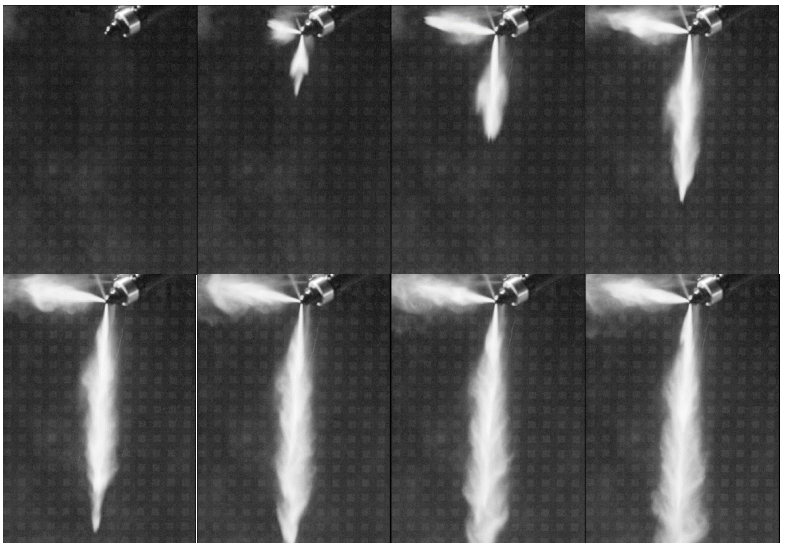

Fig. 2 D100 fuel spray
Obr. 2 Rozstrek paliva D1

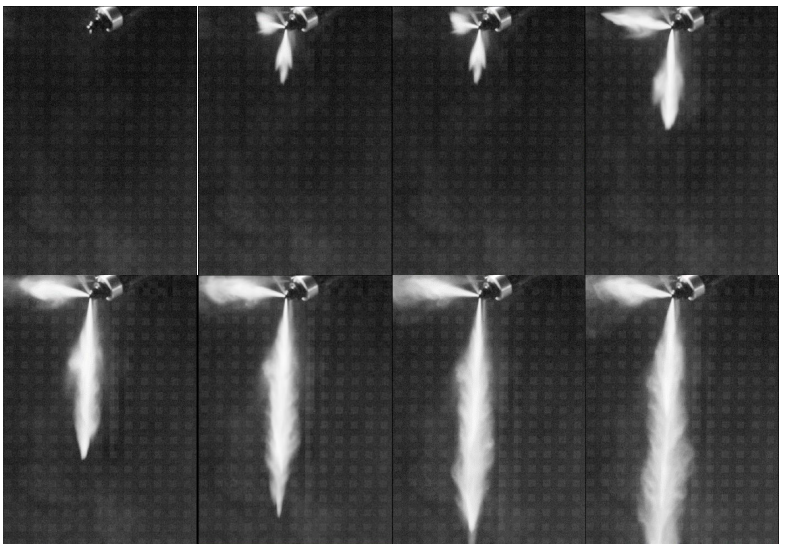

Fig. 3 Fuel spray HVO_5
Obr. 3 Rozstrek paliva HVO_5

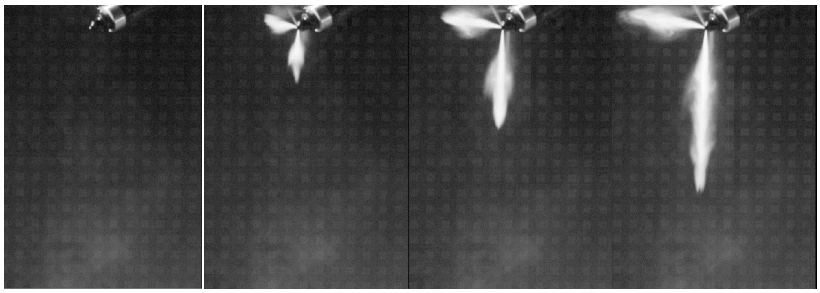

Fig. 4 Fuel spray HVO_10
Obr. 4 Rozstrek paliva HVO_10

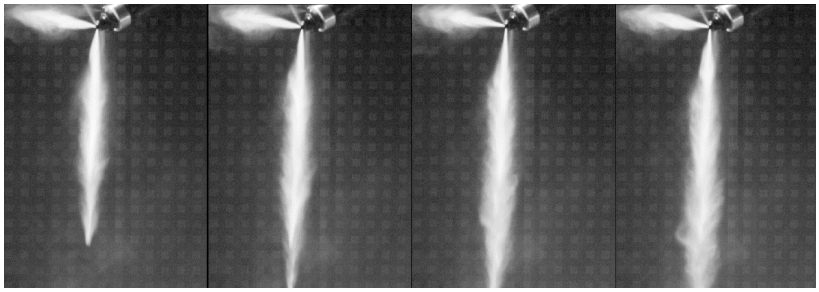

Fig.5 Fuel spray HVO_100
Obr. 5 Rozstrek paliva HVO_100

Figure 6 shows the width of the fuel spray cone for all fuels tested. It can be seen that the HVO_5 and HVO_10 fuel blends have shown very similar widths for most of the time. HVO_100 fuel, on the other hand, showed a significantly lower width, which may be associated with higher viscosity and poorer evaporation capacity of HVO. In terms of the maximum achieved width values, a decrease of 18.4% was recorded for HVO_5, 4.1% for HVO_10 and 21.2% for HVO_100.

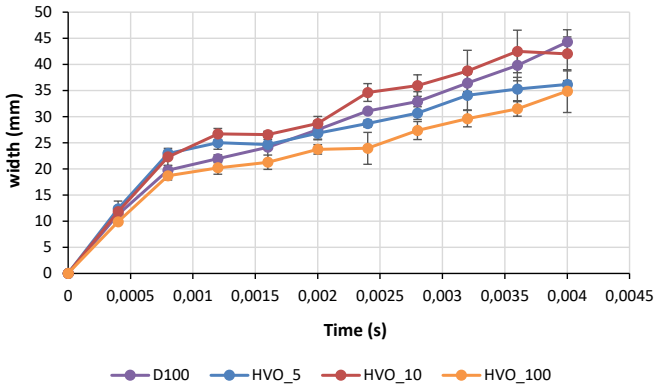

Fig. 6 Maximum sprayed fuel cone width for all fuels tested (error bars indicate standard deviation)
Obr. 6 Maximálna šírka kužeľa rozstreku pre testované palivá
(chybové úsečky indikujú smerodajnú odchýlku)

Figure 7 shows the achieved spray angle for all tested fuels, it can be seen that both mixed fuels and HVO fuel showed a significantly smaller spray angle than the reference fuel D100. This may again be due to the higher viscosity of blended fuels compared to D100. Compared to D100 fuel, the HVO_5 fuel mixture showed a decrease in the spray angle by 23.8%, HVO_10 by 19.6% and HVO_100 fuel by 28%.

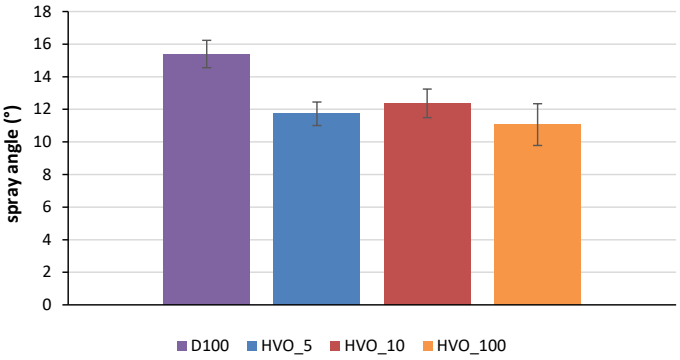

Fig. 7 Spray angle for all fuels tested (error bars show standard deviation)
Obr. 7 Uhol rozstreku pre všetky testované palivá (chybové úsečky indikujú smerodajnú odchýlku)

The spray rate of the aerosol for all fuels is shown in Figure 8. It can be seen that the velocity over time is very similar for all fuels, especially for fuels containing HVO (HVO_5, HVO_10 and HVO_100). For the D100 fuel, a lower increase in speed is seen in the second phase, following the initial opening of the nozzle. The maximum achieved aerosol spread rate was thus higher for HVO_5 fuel by 10.6%, for HVO_10 fuel by 5.1% and HVO_100 by 18%.

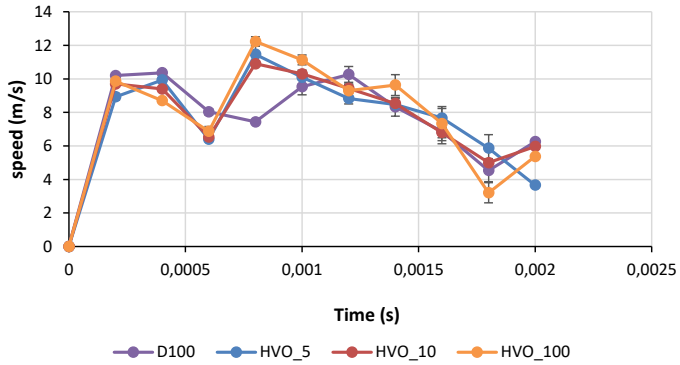

Fig. 8 Aerosol spread rate for all fuels tested (error bars show standard deviation)
Obr. 8 Rýchlosť rozstreku aerosólu pre všekty testované palivá
(chybové úsečky indikujú smerodajnú odchýlku)

Aerosol acceleration for all tested fuels as a function of time is shown in Figure 9. It is clear from Figures 8 and 9 that the injection itself takes place in at least two phases,

as can be seen from the two pronounced acceleration peaks in Figure 9. Aerosol itself can be only slow down after leaving the nozzle due to the resistance of the environment. The maximum acceleration achieved was 12.4% higher for HVO_5 fuel, 4.9% higher for HVO_10 fuel and 3.3% higher for HVO_100 compared to D100. In contrast, in terms of maximum deceleration, fuels showed significantly higher differences, for HVO_5 fuel it was higher by 51.4%, for HVO_10 fuel by 22.9% and HVO_100 by 77.1%. The course of spraying individual fuels on a series of images is shown in Figures 2-5. For each fuel, 6 images were selected to capture the course of the injection and one image as the initial one before the start of the injection. The time interval between the displayed images is approximately 0.0004 s. The images show the gradual propagation of the sprayed fuel away from the nozzle and the last 2-3 images already show the entire fuel spray cone. These images were also used to evaluate the spray angle and the maximum width of the fuel spray cone, to evaluate the speed and acceleration it was necessary to use images with a shorter time interval (approximately half), this section always captures the first 4-5 images.

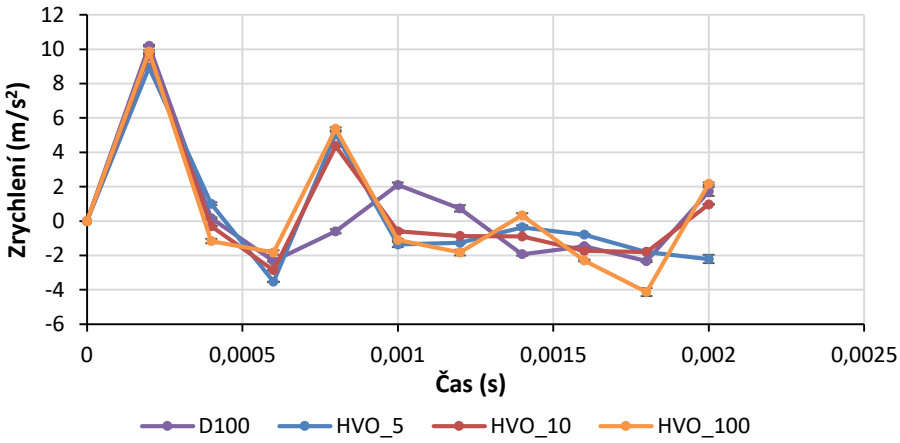

Fig. 9 Achieved aerosol acceleration values for all tested fuels (error bars show standard deviation)
Obr. 9 Dosiahnuté zrýchlenia aerosólu pre všetky testované palivá
(chybové úsečky indikujú smerodajnú odchýlku)

DISCUSSION

Very similar results were obtained in the article OPTICAL FUEL SPRAY CHARACTERIZATION OF HYDROTREATED VEGETABLE OIL, EN590 DIESEL, AND ETHANOL, which wrote Akram MS., Ainsalo A,. Anttinen T., Kaario O., Larmi M. “the spray penetration results for HVO and EN590 diesel sprays were very similar to each other; however, HVO showed a wider spray opening angle than EN590 diesel “.

CONCLUSION

The paper evaluated the spraying of hydrogenated oil in various concentrations with diesel fuel (5, 10 and 100%). Pure diesel was used as a benchmark.

– The HVO_5 and HVO_10 fuel blends showed a very similar width most of the time. HVO_100 fuel, on the other hand, showed a significantly lower width, which may be associated with higher viscosity and poorer evaporation capacity of HVO (HVO_5 by 18.4%, HVO_10 by 4.1% and HVO_100 by 21.2%).
– Both mixed fuels and HVO fuel showed a significantly smaller spray angle than the reference fuel D100 (HVO_5 by 23.8%, HVO_10 by 19.6% and HVO_100 by 28%).
– The course of the spray cone propagation rate is very similar for all fuels, especially for fuels containing HVO (HVO_5, HVO_10 and HVO_100). For fuel D100, a lower increase in speed is seen in the second phase, following the initial opening of the nozzle (HVO_5 by 10.6%, HVO_10 5.1% and HVO_100 by 18%).

The analysis of fuel spraying showed mainly the effect of higher viscosity of blended fuels and pure HVO, which is evidenced mainly by the lower measured width of the sprayed aerosol cone and the smaller spray angle compared to D100 fuel.

ACKNOWLEDGMENT

This research was funded by Internal Grant Agency of Czech University of Life Sciences Prague, Faculty of Engineering - IGA CULS - 2020: 31190/1312/3111.

LITERATURE

BIRZIETIS, G., PIRS, V., DUKULIS, I., GAILIS, M. 2017. Effect of commercial diesel fuel and hydrotreated vegetable oil blend on automobile performance. *Agronomy Research*, 15(S1), 964–970.

BOHL, T., TIAN, G., SMALLBONE, A., ROSKILLY, A. P. 2017. Macroscopic spray characteristics of next-generation bio-derived diesel fuels in comparison to mineral diesel. *Applied Energy* 186(January), 562-573.

BOHL, T., SMALLBONE, A., TIAN, G., ROSKILLY, A. P. 2018. Particulate number and NOx trade-off comparisons between HVO and mineral diesel in HD applications. *Fuel* 215, 90-101.

BORTEL, I., VÁVRA, J., TAKÁTS, M. 2019. Effect of HVO fuel mixtures on emissions and performance of a passenger car size diesel engine. *Renewable Energy* 140(September), 680-691.

ČEDÍK, J., PEXA, M., PETERKA, B., HOLŮBEK, M., MADER, D., PRAŽAN, R. 2018. Effect of biobutanol-sunflower oil-diesel fuel blends on combustion characteristics of compression ignition engine. *Acta Technologica Agriculturae*, 4, 133–138.

DIMITRIADIS, A., SELJAK, T., VIHAR, R., ŽVAR BAŠKOVIČ, U., DIMARATOS, A., BEZERGIANNI, S., SAMARAS, Z., KATRAŠNIK, T. 2020. Improving PM-NOx trade-off with paraffinic fuels: A study towards diesel engine optimization with HVO. *Fuel* 265, article no. 116921.

ELANGO, T., SENTHILKUMAR, T. 2011. Performance and emission characteristics of CI engine fuelled with non-edible vegetable oil and diesel blends. *Journal of Engineering Science and Technology* 6(2), 252–262.

ESTEBAN, B., RIBA, J.-R., BAQUERO, G., RIUS, A., PUIG, R. 2012. Temperature dependence of density and viscosity of vegetable oils. *Biomass and Bioenergy* 42, 164–171.

GAILIS, M., RUDZITIS, J., KREICBERGS, J., ZALCMANIS, G. 2017. Experimental analysis of hydrotreated vegetable oil (HVO) and commercial diesel fuel blend characteristics using modified CFR engine. *Agronomy Research* 15(4), 1582–1601.

HEIKKILÄ, J., HAPPONEN, M., MURTONEN, T., LEHTO, K., SARJOVAARA, T., LARMI, M., KESKINEN, J., VIRTANEN, A. 2012. Study of miller timing on exhaust emissions of a hydrotreated vegetable oil (HVO)-fueled diesel engine. *Journal of the Air and Waste Management Association* 62(11), 1305-1312.

HISSA, M., NIEMI, S., SIRVIÖ, K., NIEMI, A., OVASKA, T. 2019. Combustion studies of a non-road diesel engine with several alternative liquid fuels. *Energies* 12(12), article no. 2447.

HONIG, V., LINHART, Z., ORSAK, M. 2015. Use of blend of hydrotreated vegetable oil with biobutanol for applications in diesel engines. *Engineering for Rural Development* 14(January) 324-329.

CHENG, Q., TUOMO, H., KAARIO, O., MARTTI, L. 2019. HVO, RME, and diesel fuel combustion in an optically accessible compression ignition engine. *Energy and Fuels* 33(3), 2489-2501.

JOSÉ V. PASTOR, JOSÉ M. GARCÍA-OLIVER, CARLOS MICÓ, ALBA A. GARCÍA-CARRERO AND ARANTZAZU GÓMEZ: Experimental Study of the Effect of Hydrotreated Vegetable Oil and Oxymethylene Ethers on Main Spray and Combustion Characteristics under EngineCombustion Network Spray A Conditions. Appl. Sci. 2020, 10, 5460; doi:10.3390/app10165460, pp.1-20

KRIVOPOLIANSKII, V., BJØRGEN, K. O. P., EMBERSON, D., USHAKOV, S., ÆSØY, V., LØVÅS, T. 2019. Experimental study of ignition delay, combustion, and NO emission characteristics of hydrogenated vegetable oil. *SAE International Journal of Fuels and Lubricants* 12(1).

NORDELÖF, A., ROMARE, M., TIVANDER, J. 2019. Life cycle assessment of city buses powered by electricity, hydrogenated vegetable oil or diesel. *Transportation Research Part D: Transport and Environment* 75(October), 211-222.

OMARI, A., PISCHINGER, S., BHARDWAJ, O. P., HOLDERBAUM, B., NUOTTIMÄKI, J., HONKANEN, M. 2017. Improving engine efficiency and emission reduction potential of HVO by fuel-specific engine calibration in modern passenger car diesel applications. *SAE International Journal of Fuels and Lubricants* 10(3).

PECHOUT, M., MACOUN, D. 2019. Experimental investigation of combustion timing of HVO, RME and diesel fuel in a Euro6 car engine during transient driving cycles. *SAE Technical Papers* 2019(September).

PECHOUT, M., KOTEK, M., JINDRA, P., MACOUN, D., HART, J., VOJTISEK-LOM, M. 2019. Comparison of hydrogenated vegetable oil and biodiesel effects on combustion, unregulated and regulated gaseous pollutants and DPF regeneration procedure in a Euro6 car. *Science of the Total Environment* 696, article no. 133748.

PEXA, M., MAŘÍK, J., ČEDÍK, J., ALEŠ, Z. VALÁŠEK, P. 2014. Mixture of oil and diesel as fuel for internal combustion engine. In: 2nd International Conference on Materials, Transportation and Environmental Engineering. CMTEE, Kunming, 1197–1200

RIMKUS, A., ŽAGLINSKIS, J., STRAVINSKAS, S., RAPALIS, P., MATIJOŠIUS, J., BERECZKY, Á. 2019. Research on the combustion, energy and emission parameters of various concentration blends of hydrotreated vegetable oil biofuel and diesel fuel in a compression-ignition engine. *Energies* 12(15), article no. 2978.

RODRÍGUEZ-FERNÁNDEZ, J., LAPUERTA, M., SÁNCHEZ-VALDEPEÑAS, J. 2017. Regeneration of diesel particulate filters: Effect of renewable fuels. *Renewable Energy* 104(April), 30-39.

SOAM, S., HILLMAN, K. 2019. Factors influencing the environmental sustainability and growth of hydrotreated vegetable oil (HVO) in Sweden. *Bioresource Technology Reports* 7(September).

SONDORS, K., BIRKAVS, A., PIRS, V., BIRZIETIS, G., DUKULIS, I. 2019. Comparison of vehicle performance using fossil diesel fuel blends with biodiesel and HVO fuel. *Engineering for Rural Development* 18, 964-970.

SUAREZ-BERTOA, R., KOUSOULIDOU, M., CLAIROTTE, M., GIECHASKIEL, B., NUOTTIMÄKI, J., SARJOVAARA, T., LONZA, L. 2019. Impact of HVO blends on modern diesel passenger cars emissions during real world operation. *Fuel* 235(January), 1427-1435.

SUNDE, K., BREKKE, A., SOLBERG, B. 2011. Environmental impacts and costs of hydrotreated vegetable oils, transesterified lipids andwoody BTL-A review. *Energies*, 4(6), 845-877.

VOJTÍŠEK-LOM, M., BERÁNEK, V., MIKUŠKA, P., KŘŮMAL, K., COUFALÍK, P., SIKOROVÁ, J., TOPINKA, J. 2017. Blends of butanol and hydrotreated vegetable oils as drop-in replacement for diesel engines: Effects on combustion and emissions. *Fuel* 197, 407-421.

ZEMAN, P., HÖNIG, V., KOTEK, M., TÁBORSKÝ, J., OBERGRUBER, M., MAŘÍK, J., HARTOVÁ, V., PECHOUT, M. 2019. Hydrotreated vegetable oil as a fuel from waste materials. *Catalysts* 9(4), article no. 337.

ZHANG, Z., LU, Y., REN, H., ROSKILLY, A. P., CHEN, L., SMALLBONE, A., WANG, Y. 2017. Experimental and numerical investigation on the macroscopic characteristics of hydrotreated vegetable oil (HVO) spray. *Energy Procedia* 142, 474-480.

Corresponding author:
Jaroslav Mrázek, phone +420 605 025 914, e-mail: mrazekjaroslav@tf.czu.cz

DEFORMATION EVALUATION ON A FLOATING CALIPER BRAKE

HODNOTENIE DEFORMÁCIE NA BRZDE S PLÁVAJÚCIM BRZDOVÝM STRMEŇOM

Lukáš Hudec

Faculty of technology, Technical university in Zvolen, T. G. Masaryka 24, 960 01 Zvolen, e-mail: xhudecl@is.tuzvo.sk

ABSTRACT: This paper aims to evaluate deformation on a floating caliper brake in response to the hydraulic pressure of the brake fluid. Specifically, the deformation in the piston chamber is being looked. The change in volume can affect the pressure and could therefore pose a threat to the operation of the floating caliper brake. The resulting displacement of reference points between the brake caliper and the piston is then used to calculate the difference in volume after pressure is applied. Variants with different pressure values are compared. Furthermore, variants with different elements for mesh generation are used. A simplification of a brake pad in the form of a domed steel spacer is compared to a braking pad that has the compressibility behavior of a hyperfoamic material. The variants with different element types caused minimal differences in the displacement of the individual reference points and thus no significant difference in volume change. Changing the brake pads proved to be significant to the volume change. The volume change was smaller in the variant with the hyperfoam pads due to the higher compressibility of the pads. Uneven deformation could lead to uneven wear on the brake pads and their shorter lifespan.

Key words: brake caliper; deformation; element; fea

ABSTRAKT: Cieľom článku je vyhodnotiť deformáciu brzdy s plávajúcim strmeňom v reakcii na hydraulický tlak brzdovej kvapaliny. Konkrétne sa sleduje deformácia v piestovej komore, pretože zmena objemu ovplyvňuje tlak a môže preto predstavovať hrozbu pre správnu činnosť brzdy. Výsledné posunutie referenčných bodov medzi brzdovým strmeňom a piestom sa potom použije na výpočet rozdielu v objeme po použití tlaku. Porovnávajú sa varianty s rôznymi hodnotami tlaku. Ďalej sa používajú varianty s rôznymi konečnými prvkami. Zjednodušenie brzdovej doštičky vo forme klenutej oceľovej rozpery sa porovnáva s brzdovou doštičkou, ktorá má vlastnosti hyperfoam materiálu. Varianty s rôznymi typmi prvkov spôsobili minimálne rozdiely v posunutí jednotlivých referenčných bodov, a teda ani významný rozdiel v zmene objemu. Zmena objemu bola vo variante s hyperfoam podložkami menšia kvôli vyššej stlačiteľnosti podložiek. Nerovnomerná deformácia by mohla viesť k nerovnomernému opotrebovaniu brzdových doštičiek a ich kratšej životnosti.

Kľúčové slová: brzdový strmeň; deformácia; element; mkp

INTRODUCTION

FEM is a numerical method for solving physical phenomena such as stress and strain. Amidst the first submitted computational approaches for solving the discretization problem of two-dimensional stresses concerning elastic materials using a numerical solution, simple elastic bar made up the discrete model (Hrennikoff 1941; Mchenry 1943). An essential figure of the FEM was Richard Courant when in 1943, he first tried to solve the torsion problem by St. Venant. In the 1960s. Ray William Clough applied the first computational FEM and coined the term finite element in his research. While he presented his conclusions at the 2nd ASCE Conference on Electronic Computation, it had little impact on the industry at that time. The method could not be applied effectively due to a lack of sufficiently powerful computers (Clough 1960). FEA has found a large host of applications inside the automotive industry since its inception.

The main uses of FEA today in vehicle manufacturing are crash simulations, brake modeling, tire modeling. When simulating models using FEA analysis, we look for results with the greatest accuracy, shortest computing time, and shortest meshing time. In general, computing time increases with the use of a mesh with smaller elements. On the other hand, using a mesh with larger elements can cause stress values to be less accurate. A coarser mesh can be beneficial if we try to get a simplified model for an approximate and quick calculation of the effects of mesh density on the accuracy of the displacement and stress values. The proper aspect rationed mesh alone does not guarantee accurate results. The adequate density of elements is needed for accurate stress values (Javidinejad 2012). In a static simulation of a plate model, it was found that an adequate number of discretizations is about ten divisions for an approximate error under 1% (Liu 2013). The percentage of error is by far less for deflection as compared to von Mises stress. According to the Finite Element Analysis theory, stresses are not predicted as accurately as displacement (Dutt 2015). The situation gets complicated when we use different types of elements, different orders of elements, and solvers implemented in simulation software, as these have a profound impact on the results. Among the first written but never published, automated meshing solutions were available in 1958 by Mr. R. MacLean performed on the IBM 704 computer (Buell a Bush 1973). Manual meshing involves some subjective parameters such as the skill, experience, and intuition in knowing where a finer mesh is required for accurate stress values and where a coarse mesh is sufficient for increased computation time.

MATERIAL AND METHODS

An assembly of a floating caliper disc brake is used. The solver used for computation is Abaqus, and Abaqus Viewer is used for post–processing, while the mesh generation was handled using Altair HyperMesh.

The assembly variant ΔV_1 consists of the housing (1), also known as the caliper bracket, which holds the cylinder piston (2). The inner and outer backplates (3,7) are connected to inner and outer pads (4,6) and the brake disc (5). The assembly variant ΔV_g represents a simplified alternative where the inner and outer pads (4,6) are replaced by a simplified inner and outer domed steel spacer (8,9).

Material

The parts material is treated as linear elastic isotropic with its values for Young's modulus, density, and Poisson's ratio as noted in the table 1. An exemption is made for the brake pads. In order to accurately simulate the compression of such material, different compressibility based on load direction must be considered. The compressibility of brake pads is defined by how much the brake pad can be pressed together. Pad compressibility can be an essential design parameter of braking systems as it significantly impacts brake performance, comfort, and behavior that the driver experiences. It also reduces the noise and vibration that the braking system generates.

The material defnition for the pads is a compressible elastomeric foam modeled using the hyperfoam option in Abaqus. The material is defined by parameters μ_n, α_n, ν obtained from experimental test data as input. The parameters for pad inner are $\mu_1 = -283.43$, $\alpha_1 = 2$, $\mu_2 = 189.18$, $\alpha_2 = 4$, $\mu_3 = 94.46$, $\alpha_2 = -2$, $\nu_{1,2,3} = 0.12$. The parameters for pad outer are $\mu_1 = -421.52$, $\alpha_1 = 2$, $\mu_2 = 281.35$, $\alpha_2 = 4$, $\mu_3 = 140.48$, $\alpha_2 = -2$, $\nu_{1,2,3} = 0.12$

where μ_n is shear modulus [GPa]
α_n is a constant specifying the shape of the stress strain curve
ν is Poisson's ratio

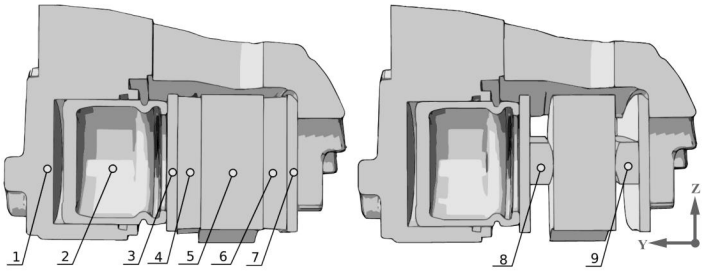

Fig. 1 Floating caliper disc brake assembly
Obr. 1 Zostava brzdy s plávajúcim strmeňom

Table 1 Material parameters
Tabuľka 1 Materiálové parametre

Pos.	Part	E	ρ	ν
1	Housing	170000	7,2	0,28
2	Piston	200000	7,85	0,3
3	Backplate inner	206800	7,82	0,3
4	Pad inner	–	2,5	–
5	Disc	115000	7,2	0,28
6	Pad outer	–	2,5	–
7	Backplate outer	206800	7,82	0,3
8	Domed steel spacer inner	210000	7,5	0,3
9	Domed steel spacer outer	210000	7,5	0,3

where E Young's modulus [N/mm^2]
ρ is the density of the material [g/cm^3]
ν is Poisson's ratio

Mesh

Quadratic and hexahedra elements have a better convergence rate than triangles and tetrahedra. It is most convenient to mesh a complex shape with tetrahedra and the second–order equivalents. However, a good mesh of hexahedral elements usually gives a solution of comparable accuracy at a lower cost. The elements used for meshing are the c3d8i element and the c3d10m. The c3d8i is a brick–type element where shear locking is removed and volumetric locking is reduced. The c3d10m is a quadratic type element with enhanced application in contact relationships. (ABAQUS Analysis User's Manual) The quality of the mesh is a crucial factor for precise stress–strain results. The quality criteria for the elements is that the max allowed angle in a quad element is 130°. The minimum allowed angle in a quad element was 30° and 20° for a triangular one. The maximum allowed skew for an element was 60, and the aspect ratio between elements was kept, so it did not exceed five.

Reference points and constraints

The reference points are set at positions to evaluate the volume change, as shown in the figure 1. The displacement on the Y–axis is used to determine the change in volume ΔV. The average of the two reference values is used for determining the length of the cylindrical volume. The piston diameter D_{piston} used is 60 mm. To assess the deformation caused during the stress–strain analysis, the change in the volume in the chamber where the cylinder piston is located is measured. Displacement can also occur at the reference points; thus, the reference position of the caliper is then subtracted.

$$\Delta l_1 = \left(\frac{u_{c1}+u_{c2}}{2}\right) - u_f \tag{1}$$

$$\Delta V = \frac{\Delta l_1 D_{piston}^2 \pi}{4} \tag{2}$$

The above equations describe nothing more than the change in volume of a cylinder with respect to the reference points from the piston and the caliper housing.

In order for the simulation to proceed, the relevant boundary conditions must be applied. The assembly is constrained by fixing the brake disc in place, symmetry constraints, and contact pairing between the parts. The assembly is symmetrical by the YZ plane. As such, the displacement in the X direction is removed together with rotations R_y and R_z using the Abaqus function "xsymm." The rest of the boundary conditions arise from the surface contacts between the assembly parts.

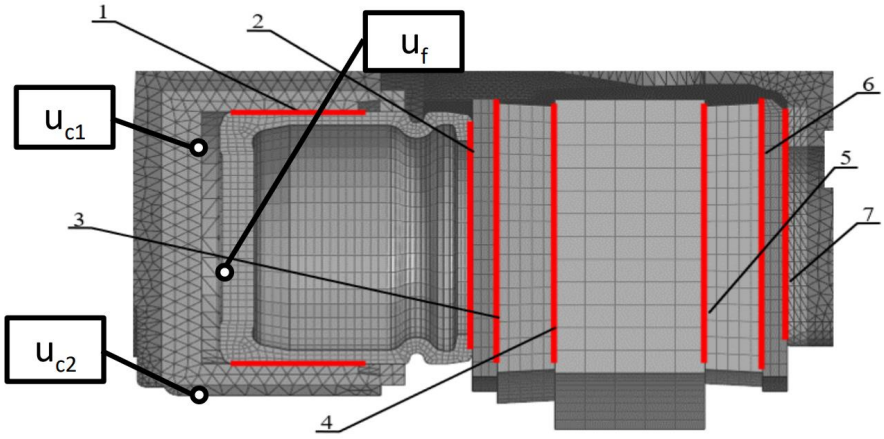

Fig. 2 Contact pairs
Obr. 2 Kontaktné páry

Table 2 Contact pairs
Tabuľka 2 Kontaktné páry

Pos.	Kontaktný pár	
1	Housing / Piston	contact
2	Piston / backplate inner	contact
3	Backplate inner / pad inner	tied
4	Pad inner / disc	contact
5	Disc / backplate outer	contact
6	Pad outer / backplate outer	tied
7	Backplate outer / housing	contact

Pressure assignment

The assembly is under load with a pressure of 100 and 160 bar. The pressure is distributed in the cylindrical space on the surfaces between the caliper and the plunger. Under actual conditions, this load would be the force of the hydrostatic pressure of the brake fluid. Pressure is applied evenly in the direction perpendicular to the elements surfaces, forming the space between the piston and the caliper. The pressure is defined using the "dsload" function by defining the area name, load type, and load pressure.

RESULTS

The result of the analysis is the deformation of the caliper brake. The total displacement of the reference points in mm is then used to calculate the change in deformation in the cylinder chamber. The deformation is measured for both variants, the ΔV_g, and ΔV_1, respectively. Variants, where different types of elements were used, were also examined.

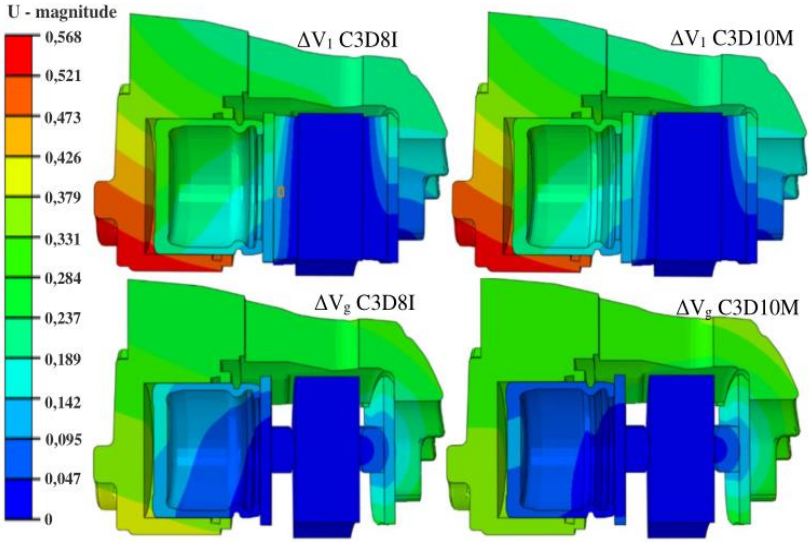

Fig. 3 Deformation magnitude
Obr. 3 Veľkosť deformácií

As shown in the figure 3, higher displacement occurs in the piston chambers bottom reference node compared to the higher positioned reference node. Therefore, the variable displacement can result in an angled piston chamber, and if this angle is significant, it could interfere with the sliding of the piston. The correct operation of the floating disc brake could be therefore hindered. The brake pads of the ΔV_1 variant are compressed more at the top, potentially leading to uneven brake pad wear. The displacements in the variant with the domed steel spacers were lower than on the brake pads with the hyperfoam material.

Evaluation of reference points

From the results in the figure, it is observed that the change in elements had a small effect on the volume change. The difference between ΔV_g c3d10m and c3d8i elements was a 0,89% increase for the 160-bar variant and an 0,78% increase for the 100-bar variant. For the V_1 variant, the difference between c3d10m and c3d8i was an 0,14% increase for the 160-bar variant and 0,16% increase for the 100-bar variant.

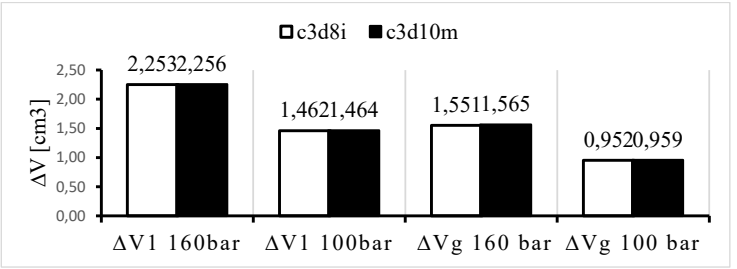

Fig. 4 Volume change results
Obr. 4 Výsledky zmeny objemu

DISCUSSION

It is known that brake pad compressibility is a measure derived from the combined elastic and plastic physical properties of the lining material. Compressibility describes the property of the pad, which depends on the material used. It is therefore in accordance with the general knowledge that the variant with the brake pads has shown higher ΔV values compared to the variant using the steel spacers.

Deformation differences due to different types of elements, produced no discernible change between the displacements of the variants, which is in accordance with the capability of the selected elements.

CONCLUSION

For the evaluation of the reference points and volume change, it is shown that the replacement of the elements caused minimal differences in the displacement of the individual reference points and thus no significant difference in volume change.

However a significant change between the variant using steel spacers and the variant with the pads was observed. The volume change is larger than the variant containing the hyperfoam pads, most likely due to the higher compressibility of the breaking pads. Uneven deformation can lead to uneven wear on the brake pads and their shorter lifespan.

ACKNOWLEDGMENT

Brake-caliper assembly and simulation software access provided by Continental Automotive Systems Slovakia s.r.o. Zvolen.

REFERENCES

BUELL, W. R. a B. A. BUSH, 1973. Mesh Generation-A Survey. Journal of Engineering for Industry. 1973, year. 95, n. 1, p. 332–338. ISSN 0022–0817. doi:10.1115/1.3438132

CLOUGH, R. W., 1960. The finite element method in plane stress analysis. 1960, p. 345–378.

DUTT, A., 2015. Effect of Mesh Size on Finite Element Analysis of Beam. International Journal of Mechanical Engineering, roč. 2, č. 12, s. 8–10. ISSN 2348–8360. doi:10.14445/23488360/IJME–V2I12P102

HRENNIKOFF, A., 1941. Solution of Problems of Elasticity by the Framework Method. Journal of Applied Mechanics 1941., s. 169–175.

JAVIDINEJAD, A., 2012. FEA Practical Illustration of Mesh – Quality – Results Differences between Structured Mesh and Unstructured Mesh. ISRN Mechanical Engineering. roč. 2012, s. 7. ISSN 2090–5130. doi:10.5402/2012/168941

LIU, Yucheng, 2013. Effects of Mesh Density on Finite Element Analysis SAE Technical Papers. roč. 2013,. doi:10.4271/2013–01–1375

MCHENRY, D, 1943. A lattice analogy for the solution of stress problems. Journal of the Institution of Civil Engineers. roč. 21, n. 2, p. 59–82. ISSN 0368–2455 doi:10.1680/ijoti.1943.13967

Corresponding author:
Lukáš Hudec, e-mail: xhudecl@is.tuzvo.sk

EFFECT OF TECHNOLOGICAL PARAMETERS ON ENERGETIC EFFICIENCY WHEN PLANAR MILLING HEAT-TREATED FOREIGN WOOD MERANTI

VPLYV TECHNOLOGICKÝCH FAKTOROV NA ENERGETICKÚ NÁROČNOSŤ ROVINNÉHO FRÉZOVANIA TERMICKY MODIFIKOVANÉHO CUDZOKRAJNÉHO DREVA MERANTI

Ľubomír Rajko, Peter Koleda, Štefan Barcík

Department of Manufacturing and Automation Technology, Faculty of Technology, Technical University in Zvolen, Študentská ulica 26, Zvolen, 960 01, Slovakia

ABSTRACT: This article deals with issues of influence of selected technical, technological and tools factors during face milling of foreign wood Meranti which is modified by temperature with emphasis on energy intensity. Experiments were conducted on samples which were modified by temperatures (160, 180, 200, and 220 °C), one of sample was in native state. Cutting conditions were: feed rate of 6, 10, 15 $m.min^{-1}$, cutting speed of 20, 40, 60 $m.s^{-1}$ and rake angle of 20, 25, 30°. Experimental measurement of cutting power was conducted via frequency converter. Effects by parameters were obtained by experiments in this order: thermally modification of material, feed rate, cutting speed

Key words: *cutting power, cutting speed, heat-treatment, feed rate*

ABSTRAKT: Tento článok sa zaoberá problematikou vplyvu vybraných technicko – technologických a nástrojových faktorov v procese rovinného frézovania termicky modifikovaného cudzokrajného dreva Meranti na energetickú náročnosť. Experimentálne meranie sa vykonávalo na vzorkách, ktoré boli termicky modifikované štyrmi termickými úpravami (T = 160, 180, 200 a 220 °C) pričom jedna vzorka bola v natívnom stave, tromi rýchlosťami posuvu (6, 10, 15 $m.min^{-1}$), tromi reznými rýchlosťami (20, 40, 60 $m.s^{-1}$) tromi uhlami čela nástroja (20, 25, 30°). Experimentálne meranie rezného príkonu sa vykonávalo prostredníctvom frekvenčného meniča. Experimentom sa získali vplyvy jednotlivých parametrov v nasledovnom poradí: tepelná úprava materiálu, rýchlosť posuvu, rezná rýchlosť

Kľúčové slová: *energetická náročnost, rezná rýchlosť, termická úprava, posuvná rýchlosť*

INTRODUCTION

Wood and its use is of great importance to humanity, whether it is the use of wood for exterior or interior. Due to outer influences, the mechanical and aesthetic properties of wood can be reduced. (Kokutse *et* al. 2006, Kaplan *et* al. 2018). Various chemicals are used to increase the resistance of wood to degradation (Kučerová *et* al. 2016), which may adversely affect the environment during production or disposal this materials (Kocaefe *et* al. 2008).

ThermoWood® is one of the most common methods of the material treatment, which achieves better physical and mechanical properties. This is a method of heat treatment of the material (Černecký *et* al. 2017), which is conducted by two standard treatments, Thermo – S a Thermo – D. Thermo – S is a process that conducts at lower temperatures and the main use is indoors and with the designation S is defined shape and dimensional stability. Thermo – D is a process which is conducted at higher temperatures, which increases the durability of the material. The essence of the thermal modification process consists of the thermal and hydrothermal treatment of wood using temperatures from 150 °C to 260 °C. With the use of high temperatures, the polymers are degraded, due to this effect the new water-soluble polymers are created. These substances are very similar to substances with a toxic or repellent effect against biological pests, such as mould or fungi (Kaplan *e. al*. 2018).

Nowadays, milling as a machining of the material is a process which has come to the fore. Milling is the process of machining using rotary cutters to remove material by advancing a cutter into a workpiece. The milling process uses a rotary tool called a milling cutter (Sedlecký *et* al. 2018, Siklienka *et al*. 2017, Lisičan 1996).

In practice, the energy intensity of the process requires high demands on the wood cutting process. The energy intensity during the milling process is influenced by various factors, such as the material of the cutting tool, the geometry of the tool, the cutting conditions or cutting power. When the material is machined, the energy intensity is often observed via cutting power (Barcík *et al*. 2009).

EXPERIMENTAL

Materials and Methods

The milling blades which were used for experimental milling had dimensions of 45 × 35 × 6 mm (h × w × t) (Fig. 1). They were made of tool steel 19 573 (STN 41 9573) and surface induction hardened. The milling blades were coated by the method PVD (Physical Vapor Deposition) in the company WOOD – B s.r.o in Nové Zámky, Slovakia. The chemical composition of the milling blades is shown in Tab. 1.

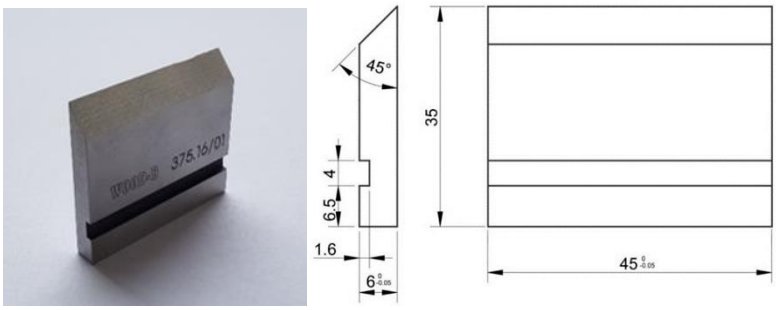

Fig. 1 Changeable milling blade
Obr. 1 Vymeniteľný frézovací nôž

Table 1 Chemical Composition of Used Milling Blades
Tabuľka 1 Chemické zloženie použitých frézovacích nožov

Blade from the tool steel 19 573							
Co	**Mn**	**Si**	**P**	**S**	**Cr**	**Mo**	**V**
1,4 ÷ 1,65	0,2 ÷ 0,45	0,2 ÷ 0,45	0,03	0,035	11 ÷ 12,5	0,6 ÷ 0,95	0,8 ÷ 1,20

The blades were clamped in the milling heads FH 45 STATON made in SZT – machines (Turany, Slovakia), with parameters mentioned in the Tab. 2.

Table 2 Parameters of Milling Head
Tabuľka 2 Parametre frézovacej hlavy

Diameter of the Cutter Body	125 [mm]
Diameter of the Cutter Body with Blades	130 [mm]
Thickness of the Cutter Body	45 [mm]
Number of Blades	2 [ks]
Maximum speed	8000 (min^{-1})
Rake Angle	γ = 20°, 25°, 30°

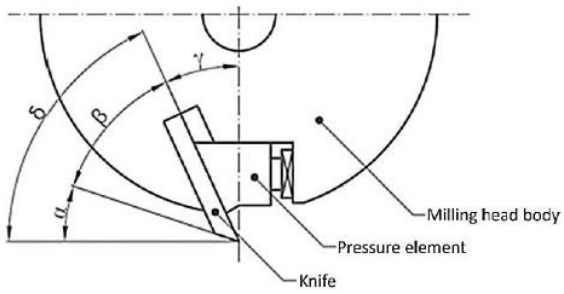

Fig. 2 Milling heads used
Obr. 2 Schéma použitých frézovacích hláv

Exotic wood of foreign origin Meranti (Shorea) from Malaysia was used as a material for the samples. From the logs, the boards of the radial medial timber with a thickness of 25 mm were manipulated on a band saw (MEBOR MTZ 1000) at a workshop of Technical university in Zvolen. The boards were dried to 10 % moisture content in a wood drying kiln. Experimental wood samples were obtained by circular saw DMMA 35 (Rema s.a., Reszel, Poland) and wood thickness planer machine F2T80 (TOS Svitavy, Czech Republic). Final cuts had dimensions: length of 700 mm, width of 100 mm and thickness of 25 mm. Part of the cuts were not treated and remained in a native state. Other cuts were thermally modified at a specified temperature. Thermally modification was conducted by ThermoWood technology. The process of thermal treatment of the material was carried out in the arboretum (ČZU Praha) in Kostelci nad Černými lesy, using a chamber S400/03 (LAC Ltd., Czech Republic). Fig. 3 shows the course of heat treatment of samples.

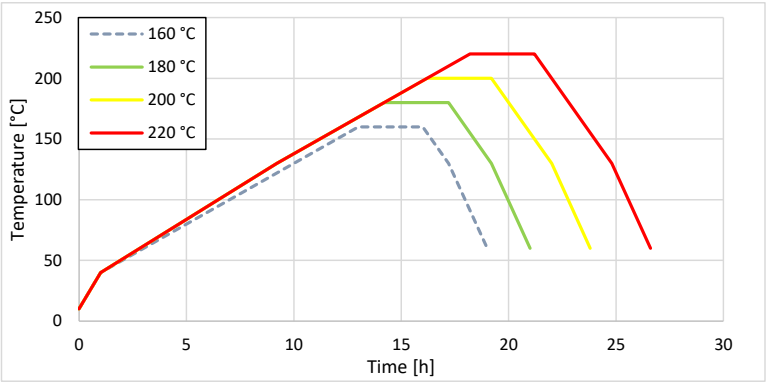

Fig. 3 Time course of heat-treatment
Obr. 3 Grafické zobrazenie tepelnej úpravy vzoriek

Fig. 4 Samples for experimental measurement
Obr. 4 Pripravené vzorky na experimentálne meranie

The milling process was performed on the lower spindle miller ZDS-2 (Liptovské strojárne, Slovakia). The feeding was ensured by the feeding device Frommia ZMD 252/137 (Maschinenfabrik Ferdinand Fromm, Fellbach, Germany). The cutting conditions were as follows: cutting speed: 20, 40, 60 m.s^{-1}, feed rate: 6, 10, 15 m.min^{-1}, rake angle: 20°, 25°, 30°.

Fig. 5 Lower spindle milling machine FVS and feeder mechanism Frommia ZMD 252/137
Obr. 5 Spodná vretenová frézka FVS s podávacím zariadením Frommia ZMD 252/137

Table 3 Technical Parameters of the Lower Spindle Miller FVS and feeding device Frommia
Tabuľka 3 Technické parameter spodnej vretenovej frézky FVS a podávacieho zariadenia Frommia

Lower spindle miller FVS		**Feeder Frommia ZMD 252/137**	
Input [kW]	4	Feed Range [m.min^{-1}]	2,5;10;15;20;30
Current System [V]	360/220	Engine [m.min^{-1}]	380 V; 2800
Year of Production	1976	Year of Production	1972

Determination of density

In order to successfully evaluate the experiment, it was necessary to determine the material density of the experimental samples according to the STN 49 0108 standard. All samples were weighted by laboratory scale with a measuring accuracy of 0,01 g and subsequent measurement by a calliper with an accuracy 0,01 mm. The resulting values of dimensions and weight of the samples were processed, and the measured values of the density was calculated according to equation

$$\rho_w = m_w / V_w \tag{1}$$

where ρ_w is the density [kg.m^{-3}],
m_w is the weight [kg],
V_w is the volume [m^3].

The average density values which are calculated from 10 values and percentage change compared to native wood are shown in table 4. The density of wood decreased with increasing heat treatment temperature; the highest density of wood was in thermally untreated wood.

Table 4 Measured Values of the Bulk Density of Wood Meranti
Tabuľka 4 Namerané hodnoty hustoty vzoriek dreviny Meranti

Thermal Treatment [°C]	Density ρ [kg.m^{-3}]	Percentage Change [%]
Native Wood	639	–
160 °C	617	3,44
180 °C	580	7,62
200 °C	559	3,62
220 °C	549	1,79

The measurement of the machine power was realised during milling of experimental samples. The frequency converter UNIFREM 400 007M (Vonsch s.r.o., Brezno, Slovak Republic) was used to measure the power input, which was connected to the computer via USB (Fig. 6). The technical parameters of the frequency converter are shown in table 5. The bottom spindle milling machine which is equipped by a three-phase asynchronous motor was controlled via a frequency changer. The power was evaluated from the current, voltage and power factor and recorded via a frequency converter without losses. The program VDS – Vonsch Drive Studio was used to graphically display the resulting values and then these values were saved to program Excel and evaluated in STATISTICA 12. From the measured data of the experiment, the results of the effects of factors via one-factorial and multi-factorial analysis were generated.

Fig. 6 Cutting power measuring apparatus
Obr. 6 Zapojená meracia sústava pre meranie príkonu

Table 5 Technical Parameters of the Frequency Changer
Tabuľka 5 Technické parametre frekvenčného meniča

Type of Frequency Converter	M – Quadratic Load		M – Constant Load				Nominal Output Current of Converter I_{nIN} [A]
	Engine Power P_{nom} [kW]	Nominal Output Current I_{NQ} [A]	Engine Power P_{nom} [kW]	Nominal Output Current I_{NK} [A]	Max. Output Current I_{NK60} [A]	Max. Output Current I_{NK2} [A]	
UNIFREM 400 007M	7,5	18,1	5,5	13,2	19,8	26,4	18,1

RESULTS AND DISCUSSION

Influence of Thermal Treatment

From Fig. 9, the highest cutting power depending on the temperature of thermal modification was at native wood. The subsequent decrease in cutting power was occurred at heat treated samples to 160 °C and 180 °C. Thermal modification of the samples to 200 °C and 220 °C increased the cutting power. According to the graph, it can be claimed that the lowest achieved value of cutting power was at the heat treatment to 180 °C.

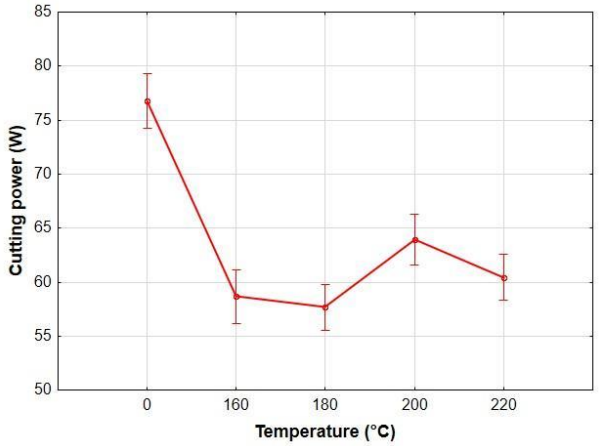

Fig. 7 Effect of thermal treatment on the cutting power
Obr. 7 Vplyv teploty termickej úpravy na rezný príkon

Influence of Feed rate

A multi-factorial analysis of the variance of cutting power dependence on feed rate is shown in Fig. 10. From the chart, the value of cutting power increases when feed rate is increased. The highest achieved cutting power was when the untreated wood was milled at feed rate of 15 $m.min^{-1}$. The lowest cutting power was achieved during milling heat-

treated sample at 160 °C at feed rate of 10 m.min^{-1}. Heat treatment of the samples at 200 °C and 220 °C causes that the cutting power at feed rate of 6 and 15 m.min^{-1} was almost the same. Almost the same cutting power was for thermally treated samples at 160 °C milled at feed rate of 6 m.min^{-1} and for thermally treated samples at 220 °C milled at feed rate of 15 m.min^{-1}.

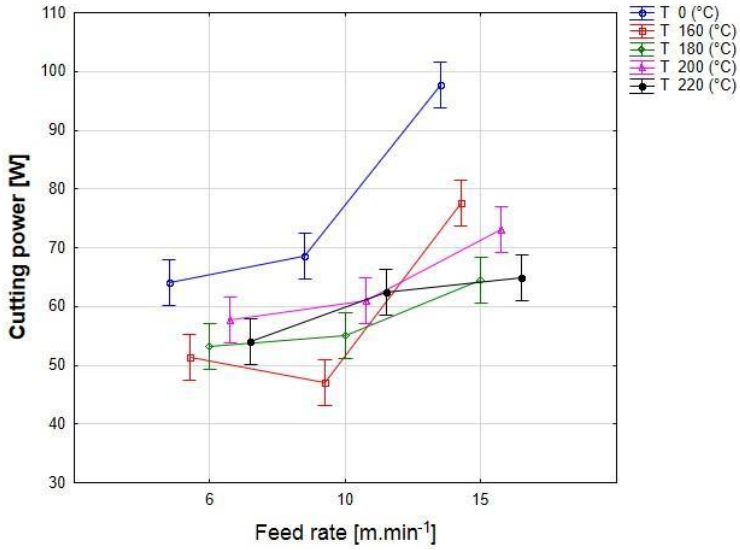

Fig. 8 Multifactor analysis of variance for the dependence of cutting power on feed rate
Obr. 9 Viacfaktorová analýza rozptylu závislosti rezného príkonu na posuvnej rýchlosti

Influence of Cutting Speed

A multi-factorial analysis of variance of cutting power influence on cutting speed is shown in Fig.11. It can be stated that as cutting speed is increased, the cutting power is increased in direct proportion. The highest cutting power was at the heat untreated sample at a cutting speed of 60 m.s^{-1}. The lowest value of cutting power was reached at the heat-treated sample at 160 °C and a cutting speed of 20 m.s^{-1}. It is further obvious from the graph that almost all heat treated samples have a constant cutting power at the highest cutting speed of 60 m.s^{-1}. At a cutting speed of 20 m.s^{-1}, the thermally modified samples at 160 °C and 220 °C have almost identical cutting power too.

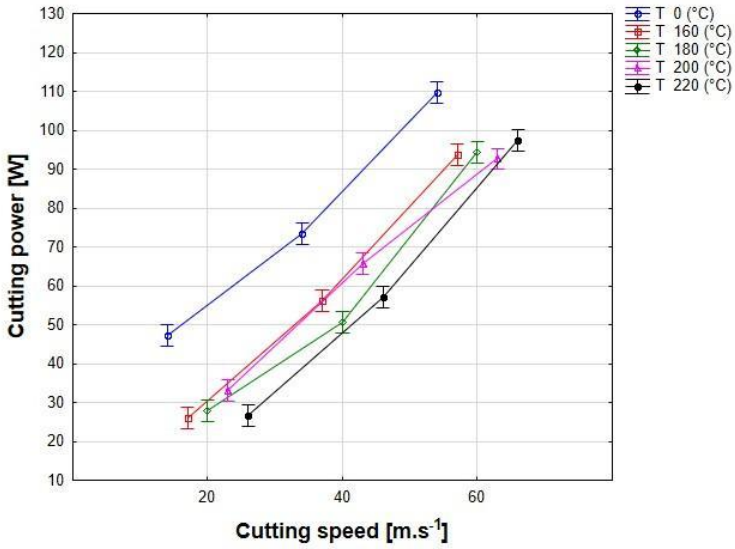

Fig. 9 Multifactor analysis of variance for the dependence of cutting power on cutting speed
Obr. 9 Viacfaktorová analýza rozptylu závislosti rezného príkonu na reznej rýchlosti

Table 6 The order of the effects of various factors on cutting power
Tabuľka 6 Poradie vplyvov sledovaných parametrov na rezný príkon

Impact on Cutting Power	Variance F	Significance Level P
Cutting Speed vc [m.s^{-1}]	3453,77	0,000
Feed Rate vf [m.min^{-1}]	356,46	0,000
Temperature T [°C]	117,5	0,000

The published article deals with an experimental study on the influence of selected technical and technological factors on energy intensity. The measurement was conducted on samples of foreign wood meranti. The results of the experiment can be compared to the authors Koleda *et al.* 2020, who researched oak wood and found that increasing the temperature of thermal modification decreases the cutting power. They further confirmed that increasing the cutting speed gradually increases the cutting power. The article also confirmed that by increasing the feed rate, the cutting power is increased excluding the thermally treated samples at 220 °C, where the highest power was achieved at a feed rate of 10 m.min^{-1}.

According to Kubš (2019), who studied oak and spruce wood, it is confirmed that increasing the cutting speed increased the cutting power. Further it was confirmed that increasing the feed rate also increases the cutting power, excluding the spruce wood where the cutting power at all feed rates was identical.

According to Jamberova (2019) the heat treatment of material had a significant effect on the cutting power, the results of measurement showed that cutting power is decreased when the temperature of heat treatment process is increased. The lowest cutting power was

achieved by the thermal modification at 220 °C. The lowest value of cutting power differs compared with our study, because we achieved the lowest power consumption when the temperature of the heat treatment process was 180°C. She also confirmed that the cutting power is increased by increasing feed rate. The results of measurement confirm that the cutting power is increased by increasing cutting speed which means that the energy difficulty is increased by increasing cutting power and feed rate too. In this case the energy intensity was measured when the modified oak wood was milled (Jamberová 2019).

CONCLUSIONS

The values of energy intensity during milling depended on the monitored factors in the following order: 1) cutting speed; 2) feed rate; 3) thermal treatment.

The cutting speed had the most significant impact on the energy intensity. Based on results which were obtained, it is recommended to use a cutting speed of 20 $m.s^{-1}$, where the lowest value of cutting power was reached in all examined samples. The highest values of cutting power were obtained at cutting speed of 60 $m.s^{-1}$ in all examined samples.

The feed rate was the second factor that affected the cutting power. Based on the thermal treatment of the wood the lowest cutting power was at the sample thermally modified at 160 °C milled at the feed rate of 10 $m.min^{-1}$. The highest cutting power was at the native sample of wood at the feed rate of 15 $m.min^{-1}$.

Temperature of the heat-treatment process of wood was one of the least significant factors that affected the cutting power. The lowest value of cutting power was obtained at a thermally treated sample at 180 °C. The highest value of cutting power was at a native sample of wood material.

ACKNOWLEDGMENTS

The paper was written within the project: VEGA 1/0315/17, "Research of relevant properties of thermally modified wood at contact effects in the machining process with the prediction of obtaining an optimal surface" the project of Internal Project Agency No. 2/2019 an the "Impact of selected technological, tool and material factors on the surface finish quality and energetic intensity at plane milling of thermally modified spruce wood" and with the support of project APVV 17/0456 "Thermal modification of wood with water vapor for purposeful and stable change of wood color".

REFERENCES

BARCÍK, Š., GAŠPARÍK, M., HOUSKA, A., RAZUMOV, E. Y., SEDLECKÝ M. 2014. Vliv technologických faktorů na kvalitu opracování povrchu při frézováni termicky modifikovaného borovicového dřeva. *Trieskové a beztrieskové obrábanie dreva* 2014. Zborník prednášok, no. 9, vol. 1, pp 11–22, 2014, ISSN 1339-8350

KOLEDA, P., BARCÍK, Š., NOCIAROVÁ, A. 2018. Effect of technological parameters of machining on energy efficiency in face milling of heat – treated oak wood. *BioResources*, no. 13, vol. 3, pp. 6133-6146. DOI: 10.15376/biores,13.3.6133-6146

JAMBEROVÁ, Z. 2019. *Analýza faktorov vplývajúcich na energetické ukazovatele pri obrábaní termicky modifikovaného dubového dreva*, Thesis. Technická univerzita vo Zvolene, Zvolen, Slovenská republika.

KUBŠ, J., GAFF, M., BARCÍK, Š. 2016. Factors affecting the consumption of energy during the milling of thermally modified and unmodified beech wood. *BioResources*, no. 11, vol. 1, pp. 736-747.

ČERNECKÝ, J., BRODNIANSKÁ, Z., BLASIAK, P. AND KONIAR, J. 2017. The research of temperature fields in the proximity of a bundle of heated pipes arranged above each other. *Journal of heat transfer* : transactions of the ASME. vol. 139, no. 8. ISSN 0022-1481.

KORČOK, M., KOLEDA, P., BARCÍK, Š., VANČO, M. 2018. Effects of technical and technological parameters on the surface quality when milling thermally modified European oak wood. *BioResources,* vol. 13, no. 4, pp. 8569-8577. DOI: 10.15376/biores,13.4.8569-8577

KUČEROVÁ, V., LAGAŇA, R., VÝBOHOVÁ, E., HÝROŠOVÁ, T. 2016. Effect of Chemical Changes during Heat Treatment on the Color and Mechanical Properties of Fir Wood. *BioResources*, vol. 11, no. 4, pp. 9079-9094. DOI: 10.15376/biores.11.4.9079-9094

MAZÁŇ, A., VANČO, M., BARCÍK, Š., RAJKO, Ľ., GOGLIA, V. 2016. Effect of angular geometry of the cutting tools for machining quality thermally mogified wood. *Chip and chipless woodworking processes*, vol. 10, no. 1. pp. 115–124, Zvolen, Technical University in Zvolen, ISSN 1339-8350

PROKEŠ, S. 1982. *Obrábění dřeva a nových hmot ze dřeva*, SNZI, Prag, Czech Republic

SIKLIENKA, M., KMINIAK, R. 2013. *Delenie a obrábanie dreva. 1. vyd.* Zvolen, Technical University in Zvolen, 207 p. ISBN 978-80- 228-2618- 1

KAPLAN, L., KVIETKOVÁ, MS., SIKORA, A., SEDLECKÝ, M. 2018. Evaluation of the effect of individual parameters of oak wood machining and their impact on the values of waviness measured by a laser profilometer. *WoodRessearch*, vol. 63, no. 1, pp. 127-140

KORČOK, M., VANČO, M., MAZÁŇ, A., BARCÍK, Š., RUDAK, P., KMINIAK, R. 2017. Influence of thermal modification of oak wood on final surface quality after plane milling. *Acta Facultatis Technicae*, vol. 22, no. 2, pp. 103–112, Zvolen, Technical University in Zvolen ISSN 1336-4472

KORČOK, M., KOLEDA, P., BARCÍK, Š., VANČO, M. 2018. Effects of technical and technological parameters on the surface quality when milling thermally modified European oak wood. *BioResources*, vol. 13, no. 4, pp. 8569-8577. DOI: 10.15376/biores,13.4.8569-8577

LISIČAN, J. (1996). *Teória a Technika spracovania dreva*, Matcentrum, Zvolen

REINPRECHT, L., VIDHOLDOVÁ, Z. 2008. *Termodrevo – príprava, vlastnosti a aplikácie*. Zvolen, Technical University in Zvolen, ISBN 978-80-228-1920-6.

SIKLIENKA, M., KMINIAK, R., ŠUSTEK, J., JANKECH, A. 2017. Delenie a obrábanie dreva. Zvolen: Technická univerzita vo Zvolene. ISBN 978-80-228-2845-1.

SIKORA, A., KAČÍK, F., GAFF, M., VONDROVÁ, V., BUBENIKOVA, T., KUBOVSKÝ, I. 2018. Impact of thermal modification on color and chemical changes of spruce and oak wood. *Journal of Wood Science*. 10.1007/s10086-018-1721-0.

Corresponding author:
Ľubomír Rajko, rajko.lubomir@centrum.sk

DESIGN OF METHODOLOGY FOR MEASUREMENT OF CHIPLLES OF CUTTING WOOD

NÁVRH METODIKY MERANIA BEZTRIESKOVÉHO DELENIA DREVA

Ján Melicherčík[1], Jozef Krilek[2]

[1]Technical university in Zvolen, Faculty of technology, T.G. Masaryka 24, 962 01 Zvolen, xmelichercikj@is.tuzvo.sk
[2]Technical university in Zvolen, Faculty of technology, T.G. Masaryka 24, 962 01 Zvolen, krilek@is.tuzvo.sk

ABSTRACT: article presents problems in wood processing in forestry. The aim of the paper is to propose a methodology for measuring chipless cutting of wood. The proposed methodology is based on theoretical and practical knowledge in the division of cutting wood. The measurement methodology is based on laboratory measurements. These are realized on experimental equipment that correspond to input and output parameters of the machine used in forestry. On the basis of the established methodology, laboratory measurements of chipless cutting of wood by means delimbing knife.

Key words: delimbing knife, harvester, cutting wood, harvester head

ABSTRAKT: článku predstavuje problematiku pri spracovaní dreva v lesnom hospodárstve. Cieľom článku je navrhnúť metodiku merania beztrieskového delenia dreva. Navrhovaná metodika vychádza z teoretických a praktických poznatkov v problematike delenia dreva. Metodika merania je založená na laboratórnych meraniach. Tie sú realizované na experimentálnom zariadení , ktoré zodpovedajú vstupným a výstupným parametrom stroja využívaného v lesnom hospodárstve. Na základe stanovenej metodiky budú realizované laboratórne merania beztrieskového delenia dreva pomocou odvetvovacích nožov.

Kľúčové slová: odvetvovací nôž, zberací stroj, delenie dreva, harvesterová hlavica

INTRODUCTION

Wood processing in forestry is greatly influenced by the development of machinery and equipment, the progress of which increases the efficiency of the process and reduces the economic costs of operation. Reducing the energy and material demands of wood processing, high reliability of machines and the incorporation of automation into this activity forces us to engage in research of the theoretical foundations of the use of forest technology in forestry (Dvořák et al. 2012). Automation and development of technology and technology is constantly developing a newer and more modern range of machines, while the processing time of wood is much faster and better. Productivity studies of timber equipment have been performed in many countries around the world, which have lasted

for more than 25 years. These studies have shown that many factors affect the productivity of individual machines (Hiesl et.al., 2013). One of the main tasks in the wood processing process is the branching of wood. It belongs to the group of chipless wood cutting. This type of operation is used on all multi-operation machines.

Delimbing is a process used to cut branches from the trunk during the processing of trees by harvester. On the main qualitative indicators such as; cutting force, cutting quality, wear resistance of the cutting edge are influenced by a large number of factors in close interdependence. In the theory of chipless wood cutting, it is known that the main component of the resistance to penetration of the knife into the wood is primarily the resistance of wood fibers to deformation, so the problem of delimbing knife heads is focused on stretching forces and their minimization and compliance with branched wood quality standards. Delimbing is an expensive item in various logging, which usually reduces the net amount of biomass recovered (Watson, 2013).

MATERIAL AND METHODS

The measurement will consist of a laboratory part, in which a jig will be used to attach a strain gauge force sensor to the experimental equipment and delimbing knives with different materials and different geometries.

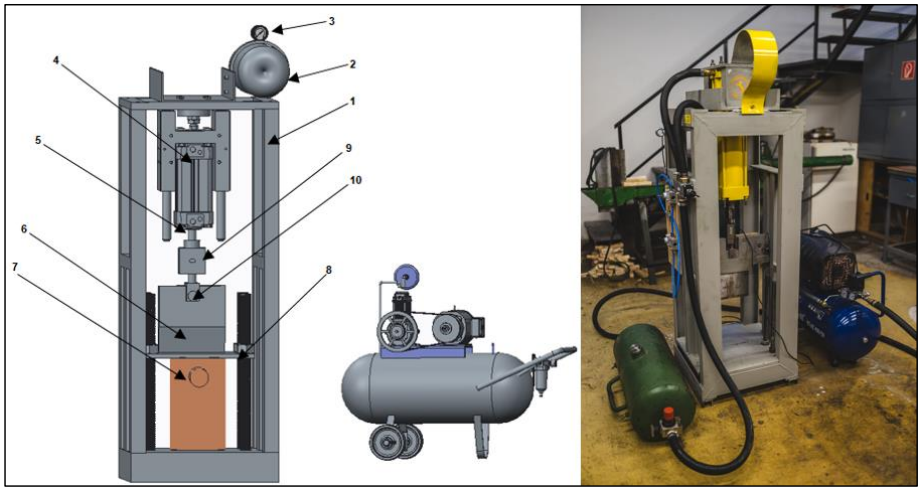

Fig. 1 Experimental equipment for chipless wood cutting
Obr. 1 Experimentálne zariadenie pre beztrieskové delenie dreva

The experimental equipment is constructed of profiled steel and shaped elements by means of welded joints. The device has dimensions of 1404 x 500 mm, the branching knife is 400 mm away from the sample material. In the upper part of the stand there is an air tank, (2) which includes a barometer (3), on which I monitor the air pressure. A pneumatic double-acting cylinder (4) with parameters according to ISO 6431 is fastened by means of a screw connection. The strain gauge pressure and tension sensor HBM S9 (9) is placed on the piston rod (5) of the cylinder by means of the designed fastening jigs (10). The

sensor is powered by connecting cables to the Quantum MX 840 measuring unit, which is an 8-channel measuring control panel. The advantage of the measuring unit is compatibility with HBM devices. The cutting device consists of a flat branching knife (6), which is located on the piston rod and is detected by a pin. After the piston rod is extended, the knife moves towards the wood sample (7), while there is a transverse division of the wood - delimbing.

The course of measurements of the laboratory part will be realized on a flat delimbing knife, which is suitable for application to our experimental equipment. Its dimensions, shape and geometry are not real compared to the pruning knife of the harvester pruning head

When dividing samples with a flat knife, the cutting force can be defined from the following relationship:

$$F_c = F_N + F_D + F_{CH} + F_{Č} = 3{,}2 + 0{,}225 + 8{,}08 + 2{,}66 = 14{,}165[\text{kN}] \quad (1)$$

where:
F_N – fcutting force by the cutting edge of the knife [kN],
F_D – deformation force of wood at the front of the knife [kN],
F_{CH} – force to overcome the resistance on the back of the knife [kN],
$F_{Č}$ – force to overcome the resistance at the front of the knife [kN].

Calculation of the force at the outlet of the pneumatic cylinder:

$$F = p.S = 600000.0{,}012265 = 7{,}359\ [\text{kN}] \quad (2)$$

Where:
F – force [N],
p – working pressure of the pneumatic cylinder [MPa],
S – area acting on the knife [m^2].

During the laboratory part, the measurement will take place in the premises of the TUZVO workshops on the experimental equipment Chipless process of splitting wood to provide a pneumatic double-acting cylinder, the end of which is attached with the help of plant delimbing knife. Laboratory measurements will be performed according to the proposed measurement chain (Fig. 3). At the beginning of the experiment, the cutting speed during delimbing is determined using a uniaxial capacitive acceleration sensor. The cutting forces required for cutting wood will be measured using the HBM S9M sensor and recorded with the Quantum MX 840 measuring units. The delimbing knives with which the experiment will be carried out are made of the material STN 19 083, whose angular geometry is according to the parameters given in Table 1. On the delimbing knives, wear will be observed after delimbing of 100 pieces of sample material from selected wood diameters. During the measurements, 2 types of sample material of spruce and Scots pine will be changed. We will determine the moisture content of the wood by the gravimetric method. From the initial measurements, we determine the most suitable angular geometry of the knife and then 3 delimbing knives will be made of stainless steel.

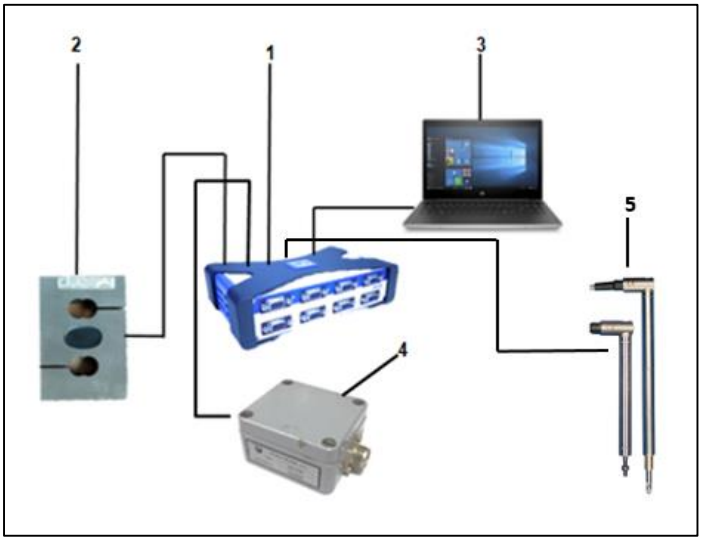

Fig. 2 Measuring chain diagram
Obr. 2 Bloková schéma meracieho reťazca
1- Quantum MX 840 measuring control panel, 2 - strain gauge strain and pressure sensor HBM S9M 20kN, 3 - PC with evaluation software, 4-axis acceleration sensor SAI / L

The wear of these knives will be detected by a conturograph or on a coordinate measuring device, which evaluates the geometric errors and deviations of the tool shape. It is a contact non-destructive method in which a cutting edge and a cutting edge radius of 0.1 mm are observed. After evaluating the energy intensity of the highest cutting force with respect to the quality of the cut, a knife with one cutting edge will be selected and will be used to produce several knives from different materials.

Delimbing knife on experimental equipment

With chipless wood cutting, the cutting tool is much simpler and more reliable compared to chain saws. Its operating costs are much lower. From research at the department (Mikleš, 2009) and from foreign analyzes (Leonov, 1990, Voronicyn and Guglev, 1989), an analysis was developed in which the parameters for wood division - branching were determined. Based on these studies and analyses of (Krilek et al., 2018) at the department, it was found that the greatest influence on the cutting resistance when it penetrates into the wood has the thickness of the branching knife. Increasing the thickness of the cutting tool increases energy consumption and deteriorates the quality of the cutting surface. Based on this, flat delimbing knives were made (Fig. 4). The basic parameters of the pruning knife are given in Table 1. For experimental measurements, a knife with a straight cutting edge will be used in order to simplify the evaluation of the cutting forces of the pruning knife.

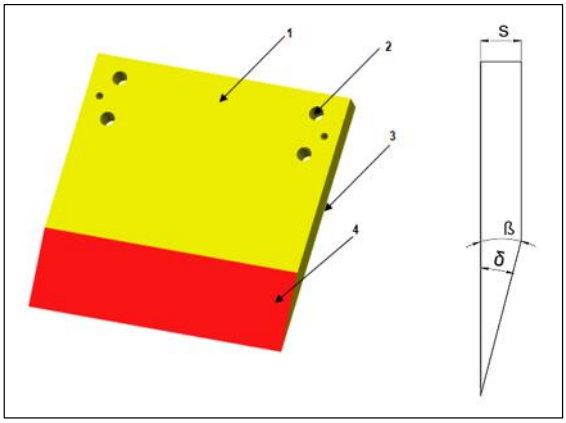

Fig. 3 Model and geometry of a branching knife on an experimental device
Obr. 3 Model a geometria odvetvovacieho noža na experimentálnom zariadení

When the pruning knife acts in the direction of the cutting forces, $\beta = \delta$ applies and no other angles (α, γ) enter the pruning process.

Table 1 Technical parameters of selected branching knives STN 19 083 (Krilek et.al., 2018)
Tabuľka 1 Technické parametre vybraných odvetvovacích nožov STN 19 083 (Krilek et.al., 2018)

P.č.	δ [°]	α [°]	s [mm]	ρ - polomer reznej hrany [mm]
1	20	7	15	0,012-0,025
2	15	4	15	0,012-0,025
3	20	4	15	0,012-0,025

RESULTS

The aim of the paper is to determine the influence of selected factors (cutting force, cutting speed, wear of pruning knives and their service life) in the process of chipless wood division – pruning on the basis of experimental measurements. Based on the processing and evaluation of the measured data, determine the weight of the influence of factors on the wear of the delimbing knife, with respect to the type of material and geometry according to which the knife will be manufactured and tested on experimental delimbing equipment.

DISCUSSION

The proposed methodology for measuring chipless wood division is based on various studies that address similar issues in the field of wood processing techniques in forestry (Mikleš J., Mikleš M., 2015, Hatton et.al., 2015, Pathak et.al., 2017). The measurement methodology consists of several factors that affect the overall life of the delimbing knife, where it is necessary to choose a suitable type of knife material (Suchánek, 2009). Based on studies (Hatton., Et.al., 2015, Hatton 2017), an experimental device for testing delimbing knives

was constructed to determine the appropriate geometry of the cutting edge of the knife. The most optimal technical parameters of delimbing knives were selected, which will be used in the next experiment (Mikleš, 2009, Krilek et.al., 2018).

CONCLUSION

The current situation in LH largely requires the use of multi-purpose forestry harvester machines in wood processing. Harvesters were used in countries with high wood production (Canada, Sweden, Finland), but over time they also reached Slovakia. In the end, this work determines the methodology of solving the dissertation with a description of laboratory measurements on experimental equipment. Based on research and theoretical knowledge, the cutting force and cutting speed will be evaluated in the branching process on the proposed experimental equipment. Delimbing knives of different geometries and different materials will be used in these measurements. In terms of cutting tool life t. j. We will determine the wear of the pruning knife by the contact non-destructive method, in which the cutting edge and the radius of the cutting edge are observed.

ACKNOWLEDGMENT

The authors are grateful for the support of the Scientific Grant Agency of the Ministry of Education, Science, Research, and Sport of the Slovak Republic, project: VEGA 1/0609/20" Research of the cutting tools at the dendromass processing in agricultural and forestry production."

This publication is the result of the project implementation:Progressive Research into Utility Properties of Materials and Products Based on Wood (LignoPro), ITMS 313011T720 supported by the Operational Programme Integrated Infrastructure (OPII) funded by the ERDF."

LITERATURE

DVOŘÁK, J., NATOV, P., HRÍB, M., NATOVÁ, L., HOŠKOVÁ, P., BYSTRICKÝ, R., KOVÁČ, J., KRILEK, J.,LIESKOVSKÝ, M. 2012. Využití harvestorových technológií v hospodárskych lesích. Kostelec nad Černými lesy,2012. ISBN 978-80-7548-028-4

HATTON, B.; POT, G.; BOUZGARROU, B. CH.; GAGNOL, V.; GOGU, G. 2015. Experimental determination of delimbing forces and deformations in hardwood harvesting, Croatian journal of forest engineering. ISSN 1845-5719, 2015, vol. 36, no. 1, pp. 43-53.

HIESL, P.,WARING, TM., BENJAMIN, JG. 2013. The effect of hardwood component on grapple skidder and stroke delimber idle time and productivity – An agent based model, Kidlington, Oxford ox5 1gb, oxon, England, Computers and Electronics in Agriculture 118 (2015) s. 270–280

KRILEK, J., KOVÁČ. J., DVOŘÁK, J., MIKLEŠ, J. 2018. Výskum rezných mechanizmov v lesníctve. Zvolen : Vedecká monografia. Technická univerzita vo Zvolene.ISBN 978-80-228-3056-0

LEONOV, A., L. 1990. Matematičeskaja model optimalizácii parametrov mechanizma prižima sučkoreznogo noža. IVUZ Lesnoj žurnal, č. 2, Archangelsk, 1990, s. 52 – 56.

MIKLEŠ, M., 2009 : Štúdium geometrie nožov odvetvovacej hlavice. Acta Facultatis Technicae, XIV , 2009 (2) : p. 121 – 129, ISSN 1136 – 4472

MIKLEŠ, J., MIKLEŠ, M. 2015. Určenie technických parametrov odvetvovacej hlavice z hľadiska

tvaru a počtu nožov : Determination of the technical parameters of delimbing head the viewpoint of their number and their shape. *Acta facultatis technicae*: vedecký časopis Fakulty enviormentálnej a výrobnej techniky. Zvolen:Technická univerzita vo Zvolene,2015,20(2),97-108. ISSN 1336-4472

PATHAK, A.D., WARHANE, R.S.,DEOKAR, S.U. 2017. Optimization of cutting parameters in Dry Turning of AISI A2 Tool Steel using Carbide Tool by Taguchi Based Fuzzy Logics. Science-Direct- Material Today: Proceedings 5 (2018) ISSN 5082- 5090

SUCHÁNEK, J., 2009. Abrazivní opotřebení kovových materiálů. 2009. [online], [cit. 05. 12. 2017]. Dostupné na internete: <http://www.tribotechnika.sk/>

VORONICYN, K. I., GUGELEV, S. M. 1989. Mašinnaja obrezka sučjev na lesoseke. Lesnaja promyšlennosť, 1989, 272 s.

WATSON W.F., TWADDLE AA., HUDSCON JB. 2013. Review of Chain Flail Delimbing-Debarking, Forest Research Institute Rotorua, New Zealand, J. B. Hudson University of Aberdeen Aberdeen, Scotland, Journal of Forest Engineerin,2013

Corresponding author:
Ing. Ján Melicherčík, PhD, Fakulta techniky,
Katedra environmentálnej a lesníckej techniky,
Študentská 26, 960 01 Zvolen, janmelichercik88@gmail.com

SELECTED INDUCTIVE FACTORS RELATED ON THE SHAPE OF OVERVOLTAGE CURRENT PULSE IN REAL CONDITIONS

VYBRANÉ INDUKČNÉ FAKTORY VPLÝVAJÚCE NA TVAR PREPÄŤOVÉHO PRÚDOVÉHO IMPULZU V REÁLNYCH PODMIENKACH

Vladimír Madola, Dušan Marko, Vladimír Cviklovič, Ondrej Lukáč

Department of Electrical Engineering, Automation and Informatics, Faculty of Engineering, Slovak University of Agriculture in Nitra, Tr. Andreja Hlinku 2, 949 76, Nitra, Slovakia, xmadolav@uniag.sk

ABSTRACT: For economic reasons, we try to minimize the effects of atmospheric surges. When developing and testing surge protectors, it is necessary to expose them to energy effects that can be compared to real overvoltage. When simulating the effects of overvoltage, a capacitive generator is most often used to generate a current pulse. We created a simulation of a current pulse, the characteristics of which we obtained experimentally. When simulating the dynamic system, we aimed to identify the possible cause of model errors. We statistically proved a significant role of the variation of the self-inductance in the transition of shock pulses through the circuit. We performed all simulations in the Matlab & Simulink environment.

Key words: dynamic system, overvoltage, current pulse, simulation, measurement error

ABSTRAKT: Účinky atmosférických prepätí sa snažíme z hospodárskych dôvodov minimalizovať. Pri konštrukcii a testovaní treba prepäťové ochrany vystaviť energetickým účinkom porovnateľným s prírodnými javmi prepätí. Pri simulovaní účinkov prepätia sa používa na generovanie prúdového impulzu najčastejšie kapacitný generátor. Vytvorili sme simuláciu prúdového impulzu, ktorého charakteristiky sme získali experimentom. Pri simulovaní dynamickej sústavy sme mali za cieľ identifikovať prípadnú príčinu chýb modelu. Štatisticky sme dokázali významnú rolu variácie vlastnej indukčnosti pri prechode rázových impulzov obvodom. Všetky simulácie sme vykonali v prostredí Matlab & Simulink.

Kľúčové slová: dynamický systém, prepätie, prúdový impulz, simulácia, chyba merania

INTRODUCTION

The phenomenon of electrical overvoltage is the subject of intensive research. Technical experience knows the mathematical approximation of shapes surge pulses in current or voltage expressions at the time. According to the literature (Rock, 2012), the current amplitude at direct impact of atmospheric discharge reaches the value of 200 kA. Time

ratios are in the order of several tens μs. In the technical conditions, generators are used to generate simulated overvoltage pulses, which are realized in the form of a capacitive battery with specific impedance (Wadhwa, 2007; Sheeba et al., 2012; Yebenbay et al., 2019).

For transients that describe the time change of the current, we can describe the given dynamic system by a linear differential equation of the 2nd order with constant coefficients.

Literature (Madola, 2020) deals in part with the research of time characteristics of overvoltage current pulses. It can be stated that at such fast transients the time derivative of time functions is significant (Madola & Lukáč, 2020). The aim of the paper is to point out the influence of the inductance of the shaping impedance on the time parameters of the current pulse of the form 10/350 μs. The results will be obtained by simulating the calculated dynamic system and are compared with the experimental data of the real device.

MATERIAL AND METHODS

Principle of overvoltage current pulse generation

A capacitive battery consisting of several capacitors arranged in parallel and charged by a DC voltage from a high-voltage DC source is used to generate the test current pulses.

The charging voltage is typically in the order of tens of kV. The basic circuit diagram is shown in Figure 1. A capacitive battery, charged to a given electrical voltage, is then discharged via shaping impedance into the test object. In the case of current waveforms, the shaping impedance is realized as a coil with a low number of turns and the cross-section of the conductor must be sufficient for resistance to current pulse stress. The active component of the impedance must be designed with respect to the time and amplitude parameters of the current pulse (Wadhwa, 2007; Halim et al., 2011; Sheeba et al., 2012; Yebenbay et al., 2019). In our work, we had a capacitive battery with a capacity of C ≈ 414 μF.

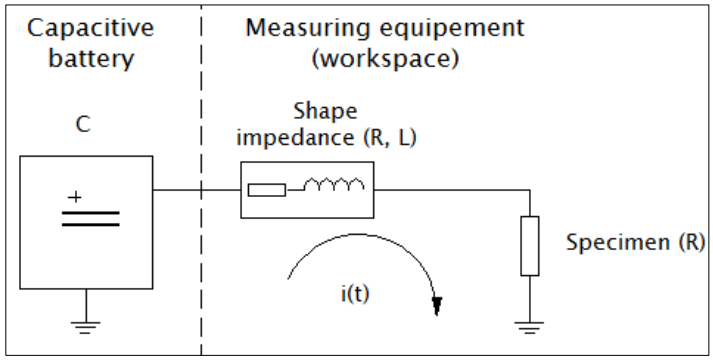

Fig. 1. Principal current pulse generator scheme
Obr. 1. Principiálna schéma generátora prúdového impulzu

Let us apply the Norton theorem to the current loop in Figure 1. For the current function we can write in the complex space the expression:

$$i(s) = \frac{U \cdot C}{s^2 \cdot L \cdot C + s \cdot R \cdot C + 1} \tag{1}$$

where $i\,(s)$ – function of electric current with complex variable [A],
U – charging voltage [V],
C – electric capacity of capacitive battery [F],
R – real part of complex impedance [Ω],
L – self-inductance of impedance [H],
s – Laplace's operator [-].

To describe the current pulse, we use a mathematical apparatus for development – a double exponential function in general form:

$$i(t) = \frac{I_m}{k} \cdot (e^{-a \cdot t} - e^{-b \cdot t}) \tag{2}$$

where $i\,(t)$ – current function with time dependence [A],
I_m – current amplitude [A],
k – wave shape factor [-],
a – coefficient of wave tail [s^{-1}],
b – coefficient of wave front [s^{-1}],
t – time [s].

When simulating the effects of overvoltage, technical practice recognizes different shapes of current pulses. A common case is the shape 10/350 μs, when the onset of the current pulse lasts 10 μs and the decline to the value of 50 % of the maximum 350 μs. This principle is used to simulate atmospheric surges on standardized tests.

The methodology of procedures for measurements using a current pulse of 10/350 μs is described in detail by a technical standard in literature (STN EN 61643 – 11, 2013).

Derivation of time constants related to experimental current wave 10/350 μs

With the use of *Rule 5τ* we can write the coefficients of front and tail of wave as follows:

$$-t_1 \cdot b \cong ln\,0.01 \tag{3}$$

$$-t_2 \cdot a \cong ln\,0.50 \tag{4}$$

where t_1 – time to reach first maximum from initial time [s],
t_2 – time to reach half of the maximum current value [s].

Let us standardize the expression (Eq. 2) by adjust to time constants:

$$i(t) = \frac{I_m}{k} \cdot \left(e^{-\frac{t}{\tau_1}} - e^{-\frac{t}{\tau_2}}\right) \tag{5}$$

where τ_1 – time constant of function fall [s],
τ_2 – time constant of function rise [s].

The solution of waveforms with a balanced share of rise and fall time is conditioned by a higher degree of damping of the rise time constant. This procedure can be applied to damped dynamic systems. Let us introduce the condition of impedance change due to electromagnetic interference in transient (Eq. 6):

$$Z = R_0 + \Delta R + jXL_0 + \Delta jXL \tag{6}$$

where Z – total impedance [Ω],
R_0 – real part of impedance on idle state [Ω],
ΔR – increase of real part of impedance [Ω],
jXL_0 – reaction part of impedance on idle state [Ω],
ΔjXL – increase of reaction part of impedance [Ω].

By solving the expression (Eq. 1) at a given electrical capacity and maximum voltage, we can change the time – amplitude characteristics of the current pulse by varying the active and reaction components of the impedance.

When oscillating to a negative polarity, the dynamic system is underdamped. Differential equation (Eq. 7) applies to voltage ration in circuit, shown on Figure 1:

$$R \cdot i(t) + L \cdot \frac{di(t)}{dt} - \frac{1}{C} \cdot \int_0^t i(t)\, dt = 0 \tag{7}$$

The underdamped dynamic system corresponding with condition (Gonos et al., 2002):

$$R < 2 \cdot \sqrt{\frac{L}{C}} \tag{8}$$

As the literature (Gonos et al., 2002) states, the solution of this differential equation is the oscillating function (Eq. 9):

$$i(t) = \frac{U}{\omega \cdot L} \cdot e^{-\alpha \cdot t} \cdot \sin(\omega \cdot t) \tag{9}$$

and substitutions are:

$$\alpha = \frac{R}{2 \cdot L}\ ;\ \omega = \sqrt{(L \cdot C)^{-1} - \alpha^2} \tag{10}$$

Practical realization of shaping impedance

The shaping (wave) impedance is realized as an air coil. The active component of the impedance must be as low as possible to minimize energy losses.

The impedance reaction component determines the rise time. The active component of the impedance together with the value of the electrical capacity of the capacitive battery determines the current course.

In our work, we used an air coil with a real impedance R = 1.10 Ω and a self-inductance, computed from geometric properties of inductor, with value L = 3.00 μH.

Typically, the shaping impedance is realized as a conductor, geometrically arranged in the shape of a coil, with active impedance in units of several Ω. The inductive part of the reactance ranges in units of several 10^{-6} H (Rock, 2012; Kamarudin et al., 2008; Eom et al., 2014).

Current pulse generator load

The capacitive overvoltage current pulse generator is used to simulate overvoltage in laboratory conditions. It is used for testing varistors, breakdown resistance of materials or, for example, for testing surge protectors according to standards.

A varistor is a non-linear electrical element that changes its instantaneous resistance depending on the applied voltage. The varistor is designed for mounting in printed circuit boards for protection of sensitive circuits against the effects of electrical overvoltage or electrostatic discharges up to the block version, designed for assembly into a block in surge protection protecting a larger electrical circuit (electrical supply for the building, secondary switchboard). If the voltage is exceeded at a current of 1 mA, the conductance will increase sharply. By raising the current to ground potential, the potentials in the circuit are equalized.

To quantify the value of the load in the experimental work, it is necessary to use Ohm's law in differential form (Eq. 11):

$$r = \frac{du}{di} \tag{11}$$

where r – immediate value of electric resistance [Ω],
du – immediate value of voltage in given time [V],
di – immediate value of electric current depending on given voltage [A].

Typically, the value of the load impedance when using a varistor in the open electrical conductivity state is in the order of several Ω. (Prasertsang et al., 2013; Sheeba et al., 2012). We used a PO I 280 V / 7 kA surge protector from the manufacturer KIWA as a load, capable of withstanding current amplitudes up to 7 kA with a current shape 10/350 μs. For simulating interference class of overvoltage, a current wave with shape 8/20 μs or 13/32 μs is used.

RESULTS

We created all simulations in the *Matlab & Simulink R2015b* environment. In the calculation case, we based on subjectively specified boundary conditions. When describing the real current course, we used the specified electrical parameters of the equipment used.

Selected results of the experiment on the used equipment

We used a current wave generator in the shape of 10/350 μs, working on the capacitive principle. As a load we used surge protection PO I 280 V / 7 kA from the manufacturer

KIWA sk. We gradually charged the capacitive battery with DC voltage up to 7.50 kV. We chose the given voltage as the maximum due to the load capacity of the given overvoltage protection by a current pulse of 10/350 μs.

When measuring the 10/350 μs current pulse, we increased capacitive battery charging voltage in steps. We measured the electrical quantities with HS4 oscilloscope with support probes. Table 1 shows experimental results: **n** – number of measurement sample, **U** – charging voltage, $\mathbf{I_m}$ – current amplitude, $\mathbf{U_r}$ – residual voltage on load, **r** - differential impedance, $\mathbf{t_1}$ – front time of current function and $\mathbf{t_2}$ – tail time of current function. The variability of times t_1 and t_2 is given in Table 2.

Table 1. Measured electrical quantities at a current pulse of shape 10/350 μs
Tabuľka 1. Namerané elektrické veličiny pri meraní prúdovým impulzom tvaru 10/350 μs

n	U [kV]	I_m [kA]	U_r [V]	r [Ω]	t_1 [μs]	t_2 [μs]
1	3.00	2.40	678.00	0.28	80.00	360.00
2	4.50	3.87	697.00	0.18	60.00	360.00
3	6.00	5.38	713.00	0.13	60.00	340.00
4	7.50	6.76	754.00	0.11	60.00	340.00

Table 2. Characteristics of variability related to front time and tail time
Tabuľka 2. Charakteristiky variability nábežného času a dobežného času

Time[1)] / Marker of variability[2)]	$\bar{x}$ [μs]	σ_s [μs]	V_K [%]	SE [μs]
t_1	65.00	10.00	15.38	± 5.00
t_2	350.00	11.55	3.30	± 5.77

[1)] Čas, [2)] Charakteristika variability

In Table 2 symbols meaning: $\bar{\mathbf{x}}$ – arithmetic mean of times, σ_s – standard deviation of sample, $\mathbf{V_K}$ – coefficient of variance and **SE** – standard error of arithmetic mean.

Simulation of current pulse from experimental data

For the simulation object we chose fourth sample from measurement in Table 1. Based on the entered data, we have derived a current function with a complex variable (Eq. 12):

$$i(s) = \frac{1}{s} \cdot \frac{3.11 \cdot s}{1242 \cdot 10^{-12} \cdot s^2 + 455.4 \cdot 10^{-6} \cdot s + 1} \tag{12}$$

By simulating the mentioned complex function (Eq. 12) in the Matlab & Simulink environment, we obtained the course shown on Figure 2 (case a).

The red point on Figure 2 (case a) shows the maximum current value in time. The blue point shows the current value at time t = 350 μs.

Differences between simulated current function and experimental data (measurement no. 4 in Table 1) are shown in Table 3.

Table 3. Differences between simulated function and experimental function of current impulse
Tabuľka 3. Rozdiely medzi simulovanou funkciou a experimentálnou funkciou prúdového impulzu

Wave[1] / Quantification marker[2]	I_m [kA]	t_1 [μs]	t_2 [μs]
Simulation[3]	6.66	14.00	330.50
Experiment[4]	6.76	60.00	340.00
Relative error[5] [%]	- 1.48	- 76.67	- 2.79

[1]Priebeh, [2] Kvantifikačný ukazovateľ, [3] Simulácia, [4] Experiment, [5] Relatívna chyba

From the results in Table 3 is obvious an extreme error at front time (t_1). The difference of 76.67 % in the case of the simulated course in comparison with the experiment is caused by the variation of the value of the reaction complexor of the shaping impedance at the transition of the shock pulse. This is justified by the transform form of Faraday's law of induction. When using the maximum limit condition to impedance (Eq. 6), the current amplitude is bounded by the unevenness $I_m < 6.82$ kA caused by real impedance vector. This makes a difference of 0.89 % from the experiment. When evaluating the character of a dynamic system, it is an overloaded system. Based on this, we can say that the solution of the characteristic equation will be two real negative roots. Decomposition into partial fractions (Rock, 2012) and inverse transformation into a time variable gives a correction relationship for substitute inductance L′ (Eq. 13):

$$L' = \tau_1 \cdot \tau_2 \cdot C^{-1} \tag{13}$$

Time constants we determined numerically by Euler attenuation rule after adjustment (Eq. 3, 4). An overview of time constants and inductance deviations is given in Table 4.

Table 4. Calculated quantification characteristics of the experimental function
Tabuľka 4. Determinované kvantifikačné ukazovatele experimentálnej funkcie

Quantification marker[1]	Value[2]
τ_1 [μs]	490.50
τ_2 [μs]	13.00
L [μH]	3.00
L‘ [μH]	15.40
δL‘ [%]	+ 413.33

[1] Kvantifikačný ukazovateľ, [2] Hodnota

Relative error δL′ in case of substitute inductance is unacceptable value. The value reached 413.33 % versus measured idle inductance.

Simulation of substitute inductance in a dynamic system

Using the current expression (Eq. 1) at the value of the substitute inductance L′ = 15.40 μH, we compiled a current function in a complex form (Eq. 14) for a dynamic system with electric capacitance C = 414 μF, real part of impedance R = 1.10 Ω and charging voltage

U = 7.50 kV:

$$i(s) = \frac{1}{s} \cdot \frac{3.11 \cdot s}{6375.6 \cdot 10^{-12} \cdot s^2 + 455.4 \cdot 10^{-6} \cdot s + 1} \tag{14}$$

By simulating the complex function (Eq. 14) in the Matlab & Simulink environment, we obtained the current course shown in Figure 2 (case b). The red point in Figure 2 (case b) shows the maximum current value in time. The blue point in Figure 2 (case b) shows the current value at time t = 350 µs.

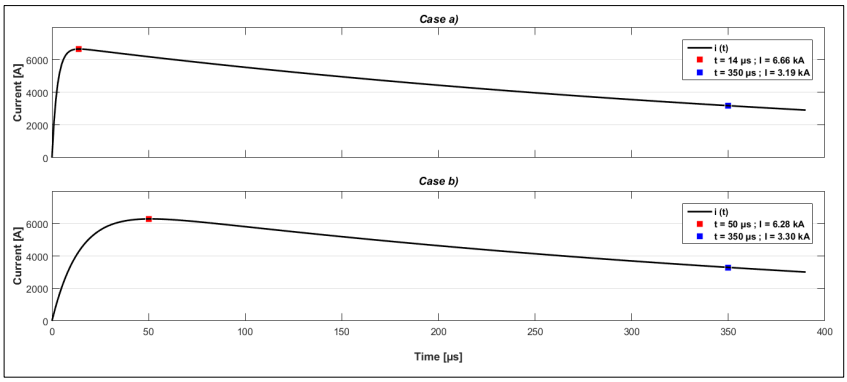

Fig. 2. Simulated complex functions of current pulses
Obr. 2. Simulované komplexné prúdové priebehy

Differences between simulated current course and experiment in Table 1 (fourth sample from measurement) are given in Table 5. The calculation of the substitute inductance L' resulted in the compensation of the relative errors of the simulated dynamic systems in comparison with the experiment. At the front time t_1, the relative error shifted by 60.00 % in the favourable direction. The relative error of the tail time t_2 increased in absolute terms by 12.05 % in an unfavourable direction. At current amplitude, the relative error increased by 5.62 % in absolute difference.

Table 5. Differences between simulated function with substitute inductance and experiment
Tabuľka 5. Rozdiely medzi simulovanou funkciou s opravnou indukčnosťou a experimentom

Wave[1] / Quantification marker[2]	I_m [kA]	t_1 [µs]	t_2 [µs]
Simulation[3]	6.28	50.00	371.50
Experiment[4]	6.76	60.00	340.00
Relative error[5] [%]	- 7.10	- 16.67	+ 9.26

[1]Priebeh, [2] Kvantifikačný ukazovateľ, [3] Simulácia, [4] Experiment, [5] Relatívna chyba

Statistical evaluation of values of time characteristics of current waveforms

Using the substitute inductance L', we were able to reduce the relative error of time t_1 by 60.00 %. At time t_2 and at current amplitude I_m, there was a slight deterioration in the error values. We compare these differences statistically at the significance level α = 0.05.

Due to the small number of measurements (n = 4), we use the test criterion for the Normal distribution using critical quantiles valid for the Student's (Gosset's) distribution.

The test statistic is in the form (Eq. 15) with respect to literature (Montgomery & Runger, 2003).

$$t_G = \frac{X - \mu_0}{\sigma_s} \cdot \sqrt{n} \tag{15}$$

where t_G – test criteria for statistic evaluation of significance [-],
X – tested statistical value,
μ_0 – medium value of the statistical set of data,
σ_s – standard deviation of sample,
n – number of repetitions.

The critical quantile for the number of measurements (n = 4) and the significance level α = 0.05 is *3.182* (Montgomery & Runger, 2003).

We formulate the main hypothesis H_0: *"The absolute values of the time parameters of current pulses differ insignificantly from their mean values"*. We formulate the alternative hypothesis H_1 in opposite to H_0: *"The absolute values of the time parameters of current pulses differ significantly from their mean values"*. To evaluate the hypotheses, we accept the condition: H_0 is accepted if $t_G \in (-3.182\,;\,3.182)$. We reject H_0 and accept the alternative hypothesis H_1 if $t_G \notin (-3.182\,;\,3.182)$. Determination of test statistics for front time t_1 and tail time t_2 is in Table 6 with results of hypothesis conclusions.

Table 6. Test statistics for hypothesis evaluation
Tabuľka 6. Testovacie štatistiky pre vyhodnotenie hypotéz

Parameter[1)]	Value[3)] (for t_1)	Value[3)] (for t_2)
μ_0 [μs]	65.00	350.00
X_1 [μs]	14.00	330.50
t_{G1} [-] / Result[2)]	- 10.20 / **H_1**	- 3.38 / **H_1**
X_2 [μs]	50.00	371.50
t_{G2} [-] / Result[2)]	- 3.00 / **H_0**	+ 3.72 / **H_1**

[1)] Parameter, [2)] Výsledok, [3)] Hodnota

From the evaluation of test statistics, we conclude on the statistically significant contribution of the substitute inductance L' in the exact description of the experimental data in the known dynamic system. At the level of significance α = 0.05, we proved the validity of the main hypothesis H_0 to the detriment of the alternative H_1 in the introduction of the substitute inductance. The test statistics for times t_2 were in favour of the alternative hypothesis H_1. From the point of view of the technical tolerance of the current pulse of a given shape, the given fact can be neglected. We chose the evaluation of current amplitudes I_m by interval estimation in the range of ± 5.00 % from the experimentally determined value I_m = 6.76 kA as interval ± 0.39 kA. From this point of view, the simulation after the introduction of the substitute inductance is outside the interval estimate.

The results of hypothesis testing directly confirm the relationship between the time deformations of the expected shape of the current pulse in the cause of the influence of the steep current on the increase of the reaction-induced voltage on the shaping impedance.

The maximum difference in current amplitude is 7.10 % and proves the relationship between the increase in the shaping impedance reaction complexor with the increase in the total impedance vector. A comparison of the relative errors shows the greater significance of the reactance complexor.

DISCUSSION

From the results, the shock increase of the reaction part of the impedance in the shaping circuit during the generation of the test overvoltage current pulses is clearly proved. The derived time constants, related to the real dynamic system, make possible to determine the effect of the change in inductance in the flow of a current pulse through the circuit. The minimal effect of voltage on the time parameters of the current pulse is statistically proven. Comparison of the initial simulations with the simulations with substitute inductance statistically significantly reduces the relative error of the rise (front) time. When designing a dynamic system with similarly defined conditions, the need for parameterization of the electrical circuit with elimination of errors is evident. Neglecting the inductance at the current flow would be an unacceptable error. In comparison with the authors (Eom et al., 2014), we can state the functional agreement of the decrease of the current amplitude with the increase of the self-inductance. At a constant value of electrical capacity, it is possible to observe a decrease in current amplitude together with an increasing instantaneous value of impedance. The authors (Gonos et al., 2002; Syahrial et al., 2016) held logarithmic increase tail time t_2 in dependence on the increasing inductance. This agrees with our previous research (Madola, 2020) where the author proves the logarithmic dependence of the current amplitude increase on the capacitance. The hyperbolic place of the time constant in the derivative of the current function in the discharge of the capacitor is a primitive function to the natural logarithm.

CONCLUSION

The paper aims to clarify the effect of variation of self-inductance at generation of overvoltage current pulses in laboratory conditions. We aimed to minimize the relative errors in the description of the real dynamic system by the transfer function in the complex plane. For the selected current form, we derived time constants by Euler's method and applied them to a theoretical model and an experimentally measured computational model. Relatively by 60.00 % and statistically at the level of significance $\alpha = 0.05$, we quantified the detected deviations causing the deformation of the current pulse by variation of self-induction in the laboratory conditions caused transient current phenomena. The results of experimental work can help in the time description of overvoltage phenomena, where technical practice uses a current curve of 10/350 μs. The results also document the use of the mathematical apparatus of dynamic functions in the description of real phenomena and the correlation in the solution of identified systems over time.

ACKNOWLEDGMENT

The experimental measurements were created with cooperation with KIWA sk company during elaboration of thesis "Analysis of construct aspects of surge protective devices".

LITERATURE

EOM, J. H., CHO, S. CH., LEE, T. H. 2014. Parameters Optimization of Impulse Generator Circuit for Generating First Short Stroke Lightning Current Waveform. *Journal of Electrical Engineering and Technology*, vol. 9, no. 1, pp. 286–292. ISSN 2093-7423.

HALIM, N. H., AZMI, A., YAHYA, Y., ABDULLAH, F., OTHMAN, M., LAILI, M. S. 2011. Development of a small scale standard lightning impulse current generator. *The 5th International Power Engineering and Optimization Conference (PEOCO)*, Selangor, Malaysia, pp. 426 – 431. DOI 10.1109/PEOCO.2011.5970422.

GONOS, I. F., LEONTIDES, N., TOPALIS, F. V., STATHOPULOS, I. A. 2002. Analysis and design of an impulse current generator. *WSEAS Transactions on Circuits and Systems,* pp. 38 – 43. ISSN 1109-2734. [online] [cit. 2021-05-02]. Available in: <https://www.researchgate.net/publication/236855552>.

HARYONO, T., SIRAIT, K. T., TUMIRAN, HAMSAH, B. 2008. The Design of A High Amplitude Impulse Current Generator. International Conference on High Voltage Engineering and Application, Chongquing, China, pp. 339 – 343. DOI 10.1109/ICHVE.2008.4773942.

KAMARUDIN, M. S., SULAIMAN, E., AHMAD, M. Z., ZULKIFLI, S. A., OTHMAN, A. F. 2008. Impulse generator and lighting characteristics simulation using Orcad PSpice software. *2nd Engineering Conference on Sustainable Engineering Infrastructures Development & Management,* Sarawak, Malaysia, pp. 1032 – 1037. [online] [cit. 2021-05-01]. Available in: <https://core.ac.uk/download/pdf/12005621.pdf>.

MADOLA, V. 2020. *Analysis of construct aspects of surge protective devices.* Diploma thesis. Nitra: SPU, 126 pp. (In Slovak: Analýza konštrukčných aspektov prepäťových ochrán).

MADOLA, V., LUKÁČ, O. 2020. Important questions related to thermal stress of surge protective devices. *Recent advantages in agriculture, mechanical engineering and waste policy*, Nitra: SPU, pp. 224 – 232. ISBN 9788055221670.

MONTGOMERY, D. C., RUNGER, G. C., Applied statistics and probability for engineers. John Wiley & Sons., 706 pp. ISBN 0471204544.

PRASERTSANG, C., TRIUATTANAPIRUK, N., YUTTHAGOWITH, P. 2013. A long duration impulse current generator for testing surge arresters in distribution systems. *10th International Conference on Electrical Engineering/Electronics, Computer, Telecommunications and Information Technology.* Krabi: Thailand, pp. 1 – 4. DOI 10.1109/ECTICon.2013.6559579.

ROCK, M., 2012. Prüfgeneratoren zur Simulation von Blitzimpulsströmen im Labor und ihre Wechselwirkung mit den Prüfobjekten. Ilmenau: Universitätsverlag Ilmenau, 294 pp.

SHEEBA, R., JAYARAJU, M., SHANAVAS, T. K. N. 2012. Simulation of Impulse Voltage Generator and Impulse Testing of Insulator using MATLAB Simulink. *World Journal of Modelling and Simulation,* vol. 8, no. 4, pp. 302 – 309. ISSN 1746-7233.

STN EN 61643 – 11. 2013. *Low voltage surge protective equipment. Part 11: Surge protective equipment involved in low voltage networks: Requirements and test methods.* (In Slovak: Nízkonapäťové prepäťové ochranné prístroje. Časť 11: Prepäťové ochranné prístroje zapojené v sieťach nízkeho napätia: Požiadavky a skúšobné metódy).

SYAHRIAL, W., NUGRAGA, S., PERMANA, Y. JR. 2016. Prototype Design and Analysis of Miniature Pulse Discharge Current Generator on Various Burdens. *International Journal on Electrical Engineering and Informatics*, vol. 8, no. 3, pp. 472 – 493. ISSN 2087-5886.

TROTSENKO, Y., BRZHEZITSKY, V., MASLUCHENKO, I. 2017. Analytical representation of switching current impulses for study of metal-oxide surge arrester models. *Technology Audit and Production Reserves,* vol. 5, no 1, pp. 24 – 29. DOI 10.15587/2312-8372.2017.109662.

WADHWA, C. L., 2007. High voltage engineering. New Delhi: New Age International, 312 pp. ISBN 9788122423235.

YEBENBAY, Y., BAIGURMANOV, A., ALIMKHAN, A. 2019. Design and simulation of automatic surge generator. 6 pp. [online] [cit. 2021-05-01]. Available on: <https://www.researchgate.net/publication/332015358_Design_and_Simulation_of_Automatic_Surge_Generator>.

Corresponding author:
Ing. Vladimír Madola, tel. 037 / 641 47 23, e – mail: xmadolav@uniag.sk

REVIEW

HOLOGRAPHIC INTERFEROMETRY AS A METHOD FOR STUDY OF HEAT TRANSFER OF THERMALLY MODIFIED WOOD

HOLOGRAFICKÁ INTERFEROMETRIA AKO METÓDA SKÚMANIA PRESTUPU TEPLA V TERMICKY MODIFIKOVANOM DREVE

Áron Hortobágyi [1], Elena Pivarčiová[2]

[1]Technical university in Zvolen, Faculty of technology, Department of manufacturing and automation technology, T. G. Masaryka 24, 960 01, Zvolen, Slovak republic, xhortobagyi@is.tuzvo.sk
[2]Technical university in Zvolen, Faculty of technology, Department of manufacturing and automation technology, T. G. Masaryka 24, 960 01, Zvolen, Slovak republic, elena.pivarciova@tuzvo.sk

ABSTRACT: The paper focuses on use of holographic interferometry as a method of heat transfer study. The method was used for observation of heat transfer from the wood surface to the surrounding air. In the experiment, spruce wood samples, thermally modified at 160 °C, 180 °C, 200 °C, 220 °C and an unmodified control sample were used. Sample was heated by radiant heat source from below. Upper face of sample was considered as observed boundary layer. Sample and ambient air temperatures were measured with use of thermocouples. The temperature fields above the sample were visualized by real-time holographic interferometry. The heat transfer coefficients α were calculated from the obtained interferograms. At the beginning of the measurement, the control sample had a heat transfer coefficient $\alpha = 16.61\ Wm^{-2}K^{-1}$. Modified samples in the order from 160 °C to 220 °C reached 88 %, 84 %, 78 %, 73 % of this value. At the end of the experiment, modified samples reached 81 %, 81 %, 79 %, 71 % of the value calculated for the control sample $\alpha = 7.64\ Wm^{-2}K^{-1}$. These values show that the thermal modification affected the heat transfer from the sample to the air. The value of the heat transfer coefficient α was lower in the modified samples than in the control samples and decreased also with the degree of thermal modification. When compared to other methods used in this field of study, results show similar patterns. This indicates that holographic interferometry could be a suitable and helpful method in this field of the research.

Key words: Thermal modification, holographic interferometry, heat transfer, thermowood

ABSTRAKT: Príspevok je zameraný na využitie holografickej interferometrie ako metódy na výskum javu prestupu tepla. Metóda bola použitá pri sledovaní koeficientu prestupu tepla na rozhraní povrchu ohrievaných vzoriek zo smrekového dreva a okolitého vzduchu. Vo výskume boli porovnávané termicky modifikované vzorky s finálnou teplotou 160 °C, 180 °C, 200 °C, 220 °C a neupravená kontrolná vzorka. Vzorka bola zospodu ohrievaná sálavým zdrojom tepla. Vrchná strana vzorky predstavovala sledované rozhranie. Teploty povrchu vzorky a okolitého vzduchu boli sledované pomocou termočlánkov. Počas experimentu boli nad vzorkou vizualizované tepelné polia, k čomu bola použitá metóda holografickej interferometrie v reálnom čase. Vyhodnotením zaznamenaných interferogramov boli vypočítané hodnoty koeficientu prestupu tepla α. Na začiat-

ku experimentu bol pre kontrolnú vzorku nameraný koeficient prestupu tepla $\alpha = 16.61$ $Wm^{-2}K^{-1}$. Modifikované vzorky v poradí od 160 °C po 220 °C dosiahli 88 %, 84 %, 78 %, 73 % hodnoty dosiahnutej kontrolnou vzorkou. Na konci experimentu upravené vzorky dosiahli, 81 %, 81 %, 79 %, 71 % z hodnoty nameranej pre kontrolnú vzorku $\alpha = 7.64$ $Wm^{-2}K^{-1}$. Takéto výsledky preukazujú, že termická modifikácia mala vplyv na prestup tepla medzi vzorkou a okolitým vzduchom. Hodnota koeficientu prestupu tepla bola pri upravených vzorkách nižšia než pri kontrolnej vzorke, taktiež bol viditeľný pokles s rastúcim stupňom termickej modifikácie. Pri porovnaní s výskumom teplotných vlastností dreva inými metódami sa výsledky pohybujú v porovnateľných medziach. Z toho sa dá usudzovať, že metóda holografickej interferometrie má potenciál ako vhodný nástroj na štúdium daného javu.

Kľúčové slová: termická modifikácia, holografická interferometria, prestup tepla, termodrevo

INTRODUCTION

Wood has been used by humans since ancient times, both for the tool production and as a building material. Due to its availability and properties, it has been used for these purposes up to this day. Some of excavated wooden tools modified by partial charring predate even the Stone Age. With this treatment, the wood acquires a higher resistance to moisture insects and fungi, which slows down its degradation and prolongs its life. To enable usage of these properties, research of the heat treatment process was raised to a scientific level.

The dimensional stability of wood during thermal modification was investigated by (Stam, Hansen, 1937). (Seborg et al., 1956) tested the properties of modified staypack wood, shaped under increased temperature and humidity conditions. (Kollmann, Scheider, 1963) focused on the absorption properties of thermally modified wood. (Burmester, 1973) investigated thermal modification as a method to improve the dimensional stability of wood. (Giebeler, 1983) also addressed this issue.

(Reinprecht, Vidholdová, 2008) investigated the mechanical properties and mold resistance of thermally modified wood. (Boonstra, 2008) described the changes in wood that occur during two-phase thermal modification of wood. (Niemz et al., 2010) studied structural changes in thermally modified wood. (Kol, Keshin, 2016) compared the thermal conductivity of wooden samples with different degrees of thermal modification. (Kol, Sefil, 2011) researched thermal conductivity of fir ad beech wood modified at various temperatures. (Korkut et al., 2013) studied effects of heat treatment on surface characteristics of wild cherry wood. (Olarescu et al., 2015) researched thermal conductivity of solid wood panels made from heat treated spruce and lime wood strips. (Pásztory et al., 2017) led a research on effect of heat treatment duration on thermal conductivity of spruce and poplar wood. (Czajkowski et al., 2020) studied effect of heat treatment on thermal properties of European beech wood. (International thermowood association 2003) summarized information about ThermoWood process and its effects on modified wood.

(Barcík, Gašparík, 2014) dealt with the influence of the tool and the parameters of abrasive machining on the chip size of thermally modified wood. (Kol et al., 2015) observed a change in the properties of wood that has been modified at different temperatures. (Kubs et al., 2017) investigated the effect of thermal modification of pine wood on the energy consumption of a milling machine. (Koleda et al.,2018) solved a similar topic, with samples from spruce wood and (Korčok et al., 2018) compared the quality of milled surfaces on samples modified at different temperatures.

(Cui, Matsumura, 2019) observed changes in the color of the surface of thermally modified wood during the weathering process. (Kačíková et al., 2020) dealt with the change of lignin in wood due to thermal modification. (Kminiak et al., 2020) investigated the particle size distribution from sawing and milling of thermally modified wood.

As it is already known, intensity of heat conduction in wood depends on anatomic direction, in which it is measured (it is highest in longitudinal direction). Heat transfer study in three anatomic directions of wood (radial, tangential, longitudinal) for four species of wood (beech, oak, spruce, poplar) has been done in detail by (Pivarčiová, 2002). Effects of wood structure direction (radial, tangential, longitudinal) on intensity of heat transfer through beech wood samples was researched by (Pivarčiová et al., 2019). In both cases, subject of study was heat transfer through unmodified wood. This article is focused on research of heat transfer through wood modified by ThermoWood method, with use of holographic interferometry.

In this research, temperature fields over heated thermowood samples were observed. Main objective was to gain new information about properties of this material, mainly time dependencies, *continual* course of heat transfer and overall survey of temperature field.

Other objective was use of method of holographic interferometry in this field of study, with aim to gain results comparable to methods already in use.

Therefore, visualization of temperature fields was done by holographic interferometry. This enabled visualization of temperature fields and real-time tracking of events at boundary layer wood-ambient *environment* without affecting process by measuring devices.

Heat transfer coefficient α [Wm-2K-1] describes thermal energy transferred between solid surface and ambient fluid. Value of this coefficient depends on size and shape of surface, as well as on *properties* of fluid and aerodynamic state of it. In general, the coefficient α can be described as a function of parameters (Kossaczký, Surový, 1963):

$$\alpha = f\,(w, \rho, \mu, c_p, \lambda, \beta, g, \tau, t_w, t_w, l_1, l_2, \ldots), \tag{1}$$

where w – velocity, ρ – density, μ – dynamic viscosity, c_p – specific heat, λ – thermal conductivity, β – coefficient of thermal expansion, t_f – fluid temperature, t_w – wall temperature, τ – time, l_1, l_2 – characteristic geometric dimensions.

During our experiments, *temperature* difference between sample surface and air ranged from 18,4 °C to 41 °C.

MATERIAL AND METHODS

Sample preparation

Samples of spruce (picea abies L.) wood were used for the research. Tree was cut in Slovakia at an altitude of 440 m. At the Technical University in Zvolen, lateral radial planks with longitudinally oriented grain with dimensions of 20 × 100 × 700 mm were sawn from the log and then dried to moisture content of 8 %. After drying, samples were heat treated in the FLD Arboretum (CULS Prague) in Kostelec nad Černými lesy. Heat treatment was conducted by ThermoWood method, with use of S400 / 3 kiln (LAC Ltd.,

Czech Republic). The heat treatment was set to final temperatures of 160, 180, 200 and 220 °C with final moisture content of 4–7 %. An untreated plank from the raw material was left, as a source of control samples. When loaded into the kiln samples were at temperature of 10 °C. Sample temperature at their removal from kiln was and at 40 °C.

Temperatures *and* time intervals of thermal modification and sample densities are listed in Table 1. Fig. 1 shows the modification course of the samples used in this experiment.

Table 1. Time intervals of thermal modification of spruce samples with final densities (Hrčková et al., 2018)
Tabuľka 1. Časové intervaly termických modifikácií smrekových vzoriek a hustoty upravených vzoriek (Hrčková et al., 2018)

Final temperature (°C)	I. phase (h)	II. phase (h)	III. phase (h)	IV. phase (h)	V. phase (h)	VI. phase (h)	Sum (h)	Final density (kg.m^{-3})
Natural	–	–	–	–	–	–	–	442
160	1.0	6.9	3.0	3.0	1.2	1.8	16.9	431
180	1.0	7.5	4.5	3.0	2.0	1.8	19.8	409
200	1.0	6.9	6.4	3.0	2.8	1.8	21.9	372
220	1.0	7.5	8.2	3.0	3.6	1.8	25.1	363

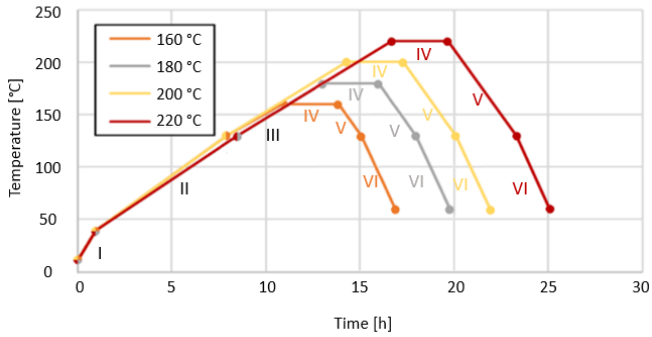

Fig. 1. Course of thermal modification of samples used in experiment (Hrčková et al., 2018)
Obr. 1. Priebeh termických modifikácií vzoriek použitých v experimente (Hrčková et al., 2018)

After heat treatment, 40x40x10 mm samples were cut from planks, five for each final temperature, as well as five untreated control samples. Samples are shown in Fig. 2.

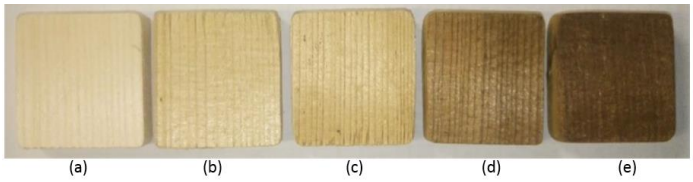

Fig. 2. Samples of natural (a) and heat-treated spruce wood at 160 °C (b), 180 °C (c), 200°C (d), 220 °C (e).

Air temperature was kept at 23 °C during the experiment. To enable formation of layers of air of different density, as seen on Fig. 4, absence of movement of ambient air, as well as constant moisture content was a necessity.

Heat transfer coefficients and surface roughnes of samples were not measured in this study.

Holographic interferometry device set-up

A holographic variant of the Mach-Zehnder interferometer as shown in Fig. 3. was used. This variant is one of the most used devices for visualization and measurement of two-dimensional transparent objects. It can be set to a finite or infinite width of light beams.

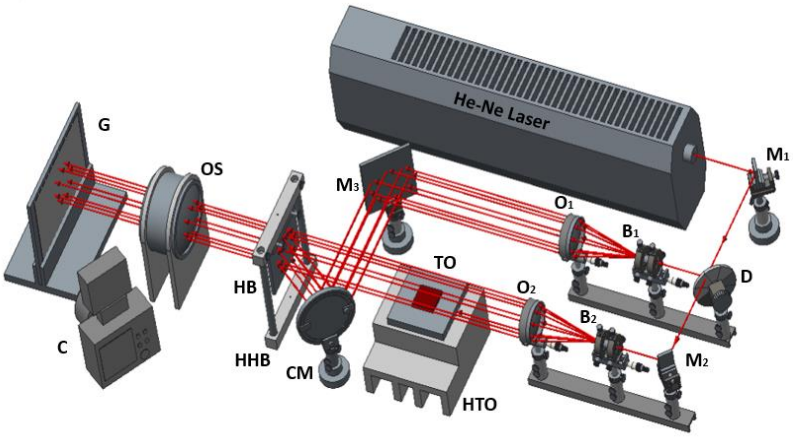

Fig. 3. Schematic of a holographic variant of a single-wave Mach-Zehnder interferometer (Pivarčiová et al., 2019): OL – object line, RL – reference line, D – divider, HB – holographic board, HHB – holder of holographic board, CM – mirror in cardan suspension, O1, O2 – object lenses, M1, M2, M3 – mirrors, B1, B2 – perforated blinds, MO1, MO2 – microscopic object lenses, TO – testing object, HTO – holder of the testing object, C – Camera, G – ground glass, Os – system of object lenses

Obr. 3. Schéma holografického variantu Mach-Zehnderovho interferometra (Pivarčiová et al., 2019): OL – predmetový lúč, RL – referenčný lúč, D – delič, HB – holografická doska, HHB – držiak holografickej dosky, CM – zrkadlo v kardanovom závese, O1, O2 – objektív, M1, M2, M3 – zrkadlá, B1, B2 – dierková clona, MO1, MO2 – mikroobjektív, TO – testovaná vzorka, HTO – držiak testovanej vzorky, C – fotoaparát, G – tienidlo, Os – sústava objektívov

A He-Ne laser with a wavelength $\lambda = 0.6328 \cdot 10^{-6}$ m, with continuous illumination and a power of 50 mW was used as the source. After reflection from the mirror (M_1), the beam on the divider (D) is split into a reference and an object beam. These beams are led through optical systems composed of a micro-lens (MO_1, MO_2), an aperture (B_1, B_2) and an objective (O_1, O_2). Optical systems are designed to widen the laser beams.

After passing through the micro-lens (MO_1, MO_2), the narrow light rays are changed into a spherical wave. Perforated screens (B_1, B_2) are designed to filter out higher bending orders, for elimination of bending and interference effects caused by impurities of previous optical elements.

At the end of the system lens (O_1, O_2) alter shape of waves from spherical to planar. Optical system for the subject beam has a small focal length with small diameter and larger focal length with larger lens diameter are used for the reference beam.

Testing object (TO) *mounted* on holder (HTO) is placed in objective beam branch. Light beam passes over the test body and illuminates the holographic plate (HB), which is placed in the holder (HHB).

Reference beam is *reflected* by a mirror (M_3) and a mirror in cardan suspension (CM) and illuminates the holographic plate (HB). The mirror (CM) can be rotated to switch the bandwidth setting in the reference area to either finite or infinite.

Interference patterns are *projected* through the lens system (OS) onto the ground glass (G), where they are recorded by a camera (C).

A radiant heat source, wrapped in heat-resistant insulating material, is placed under the holder of the testing object (HTO). This heated testing object from below in such way, that heated air could not escape around the sample.

During the experiments, *the* air temperature in laboratory was 23 °C.

The Vibra program *developed* at the Technical University in Zvolen was used for evaluation of resulting interferograms and for calculation of heat transfer coefficient.

Analysis of holographic interferograms

The analysis of holographic interferograms was based on the assumption, that the refractive index of light is *constant* along each beam. Thus, the experiment can be considered twodimensional. Conversion of the refractive index of light to absolute temperature is possible using the Gladston-Dael relation:

$$n = K\rho + 1, \tag{2}$$

where K – constant depending on the type of gas, n – refractive index of light and ρ – density, which is proportional to the pressure P and the temperature T. The relation (2) interconnects the refractive index with the density of the gas. Since both are state parameters, relation (2) is equation of state of an ideal gas.

For dry air and He-Ne *lasers* with light wavelength $\lambda = 632.8$ nm, refractive index of light can be described by (Černecký, Pivarčiová, 2011):

$$\partial n/\partial T = 7.8607 \cdot 10 - 7 \cdot p/T2, \tag{3}$$

where n – refractive index, p – air pressure, T – air temperature.

For quantitative evaluation of interferograms, it is necessary to know their relations. Their derivation from the mathematical description of the origin of interferometry was described by (Černecký, Pivarčiová, 2011). The change in the optical paths of the light

beam during the transition through optical inhomogeneity can be described by the equation:

$$\Delta o\ (x, y) = l[\Delta n\ (x, y) - n_{\infty}], \tag{4}$$

where Δo – difference of optical paths, l – length of model, $n\ (x, y)$ – refractive index at location x, y of phase object, n_{∞} – refractive index in reference area (refractive index of measuring medium without phase object).

When the *reference* and subject waves interfere, an interferogram occurs. For change the interference order ΔS (x, y) applies:

$$\Delta o\ (x, y) = \Delta S\ (x, y) \cdot \lambda, \tag{5}$$

where Δo – difference of optical paths, λ – wavelength of light, $\Delta S\ (x, y)$ – change of interference order.

Interferometric research by deriving from the change of the refractive index of light provides the possibility to calculate the values of physical quantities in the monitored transparent object. With assumption that pressure has a constant value, heat distribution can be evaluated directly from the interference order.
Its change has *integer* values in the places of light fringes:

$$\Delta S\ (x, y) = -n; \ldots; -3; -2; -1; 0; 1; \ldots; n$$

and in places of dark fringes:

$$\Delta S\ (x, y) = \ldots; -3.5; -2.5; -1.5; -0.5; 0.5; 1.5; \ldots$$

This method of assigning the interference order applies when the interferometer is set to the infinite width. In such case, objects are parallel with the reference wave in the homogeneous part of the object and no *change* in the interference order ($\Delta S\ (x, y) = 0$) occurs.

The refractive index n (x, y) is calculated at the observed location as a function of refractive index in the reference region n_{∞}, *change* of the interference order $\Delta S\ (x, y)$, light wavelength λ and length of the model l. Equation derivation is based on assumption, that deviation caused by the observed inhomogeneity is negligible and displacement of the light beam has the shape (Černecký, Pivarčiová, 2011):

$$n\ (x, y) = n_{\infty} + \Delta S\ (x, y) \cdot \lambda / l, \tag{6}$$

where $n\ (x, y)$ – refractive index at the location x, y of the phase object, n_{∞} – refractive index in the reference region, $\Delta S\ (x, y)$ – change of the interference order, λ – wavelength of light, l – length of the model.

For evaluation of *interferograms*, it is necessary to know the dependence between state quantities of the object and distribution of refractive index in the optical inhomogeneity that occurred during their change.

Dependence of *temperature* on the state variables of the environment, on the length of the model, wavelength of light and on the number of dark fringes between the object and the place of homogeneous environment can be determined according to (Černecký et al., 2012):

$$T(x, y) = T_{\infty} / [1 - 0.805 \cdot (T_{\infty})/(l \cdot p_{\infty}) \cdot (s - ½)], \quad (7)$$

where $T(x, y)$ – temperature distribution, T_{∞} – air temperature in the reference area, p_{∞} – pressure in the given space, s – interference order, l – length of the object.

Calculation of heat transfer coefficient

The heat transfer *coefficient* α [$Wm^{-2}K^{-1}$] represents the amount of heat that transfers from the surface of the body to the fluid. It is thus used for phenomena at the interface of a solid with a fixed arrangement of particles and a fluid in which there is a constant relative movement of the particles. In our case, the solid object is a wooden sample, and the fluid is ambient air. The value of the coefficient depends on the dimensions and shape of the wall, the properties of the fluid and the hydrodynamic conditions in the fluid.

When adjusted, this equation gains form (Kossaczký, Surový, 1963):

$$\alpha = (\lambda / l) \cdot f' \cdot (Fo, Re, Gr, Pr, l_1/l_2) \quad (8)$$

where λ – heat conductivity coefficient, l – wall thickness, *Fo* –Fourier criterion, *Re* – Reynolds criterion *Gr* – Grasshoff criterion *Pr* – Prandtl criterion

If it is necessary to determine *the* local value of the heat transfer coefficient, it can be done using the equation (Černecký, Pivarčiová, 2011):

$$\alpha x = -\lambda v \cdot (\Delta T / \Delta y)x \cdot 1 / (Tx - T_{\infty}), \quad (9)$$

where λ_v – coefficient of thermal conductivity of ambient air (for dry air at 20 °C, $\lambda_v = 2{,}524\ W \cdot m^{-1}k^{-2}$), $(\Delta T / \Delta y)x$ – derivation of temperature at position x, Tx – body surface temperature at point x, T_{∞} – ambient temperature.

Since the analysis of interferograms enables determination temperature distribution in the fluid in detail, method for *calculation* of heat transfer coefficient from temperature derivatives is a useful tool in interferometric heat transfer research.

Data selection

Method of holographic *interferometry* was used in the experiment, which allowed the visualization of the distribution of temperature fields over the heated sample. To be able to get useful data from the interferograms, it was necessary that they contain at least two interference fringes. This required a sufficient temperature difference between the sample and the ambient air. This condition was met at the 12th minute of sample heating.

RESULTS

During the *heating* of the samples, heat transfer occurred, and a thermal boundary layer formed above the sample. Interference fringes formed in this layer. At low temperatures, there were few fringes, their number increased during the experiment. This sequence is shown in Fig. 4.

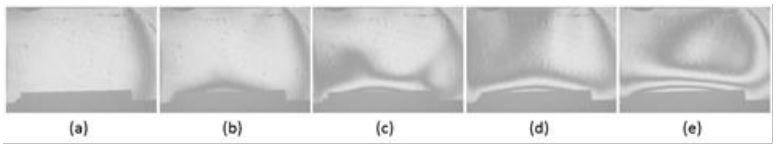

Fig. 4. Sequence of formation of interference fringes during heating. (a) Sample at the beginning of heating, (b) Formation of the first fringe, 6 min. (c) Beginning of the formation of the second fringe, 13 min. (d) Fully formed second fringe, 15 min. (e) Three visible fringes, 22 min.
Obr. 4. Postupnosť vytvárania interferenčných prúžkov počas ohrevu vzoriek. (a) Vzorka na začiatku ohrevu. (b) Vytvorenie prvého interferenčného prúžku po 6 minútach ohrevu. (c) Začiatok formovania druhého interferenčného prúžku, 13 minút ohrevu. (d) Plne vytvorený druhý interferenčný prúžok, 15 min. (e) Tri viditeľné interferenčné prúžky, 22 min.

Interference patterns were projected onto a screen and recorded with the camera at 15 s intervals. From *obtained* images, two samples per minute intervals were chosen. To evaluate the data in the image, at least two interference fringes had to be present. Records from the range of heating time 12–25 min met this criterion. The temperature profile of the thermal boundary layer above the sample was obtained by analysis of interferograms using the Vibra program. The program used the implemented formulas (7) for calculation of the temperature, and (9) for calculation of heat transfer coefficient. Each interferogram was analysed at section at section with highest points of fringes as close to sample centre (at x axis) as possible.

In Fig. 5. an example of the evaluation of the temperature profile above the sample is shown.

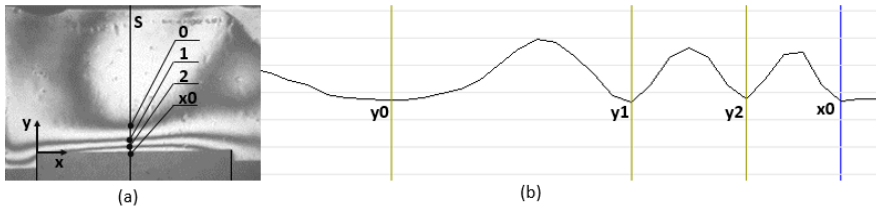

Fig. 5. Evaluation of the temperature profile above the sample (spruce treated at 200 °C, surface temperature 66.58 °C). (a) Evaluated interferogram indicating the section line (S), (b) Marking the position of the interference fringes (y0; y1; y2) and the surface of the heated sample (x0).
Obr. 5. Vyhodnotenie teplotného profilu nad vzorkou (smrek modifikovaný pri 200 °C, teplota povrchu 66,58 °C. (a) Vyhodnocovaný interferogram s vyznačením línie vyhodnocovania, (b) označenie polohy interferenčných prúžkov (y0; y1; y2) a povrchu zohrievanej vzorky (x0).

The dependencies of the heat transfer coefficient on the heating time with sample surface temperatures are summarized in Table 2. Dependencies are graphically illustrated in Fig. 6. The percentual differences of the resulting values compared to the control sample are summed up in Table 3.

Table 2. Calculated values of the heat transfer coefficient α and sample surface temperatures
Tabuľka 2. Vypočítané hodnoty koeficientu prestupu tepla α a teploty na povrchu vzoriek

	Heat transfer coefficient α / surface temperature *[°C]*									
Heating time [min]	**Final temperature of heat treatment [°C]**									
	natural		160		180		200		220	
12	16.61	*42.5*	14.65	*41.4*	14.00	*41.4*	12.88	*41.4*	12.06	*41.4*
15	–	–	13.89	*47.9*	13.61	*47.9*	9.78	*47.9*	8.75	*47.9*
17	15.57	*48.0*	13.30	*49.6*	12.34	*49.6*	8.20	*49.6*	8.07	*49.6*
19	12.05	*52.3*	10.66	*54.4*	10.47	*54.4*	7.44	*54.4*	7.02	*54.4*
21	10.65	*58.6*	9.71	*56.3*	9.39	*56.3*	6.47	*56.3*	6.50	*56.3*
23	8.10	*62.9*	6.77	*59.3*	7.07	*59.3*	6.39	*59.3*	5.99	*59.3*
25	7.64	*65.0*	6.20	*61.9*	6.18	*61.9*	–	–	5.42	*61.9*

Table 3. Comparison of the values of the heat transfer coefficient α of thermally modified samples to the control sample
Tabuľka 3. Porovnanie hodnôt koeficientu prestupu tepla α upravených vzoriek voči kontrolnej vzorke

	Final temperature of heat treatment [°C]				
Heating time [min]	**natural**	**160**	**180**	**200**	**220**
	100 %	88 %	84 %	78 %	73 %
17	100 %	85 %	79 %	53 %	52 %
19	100 %	88 %	87 %	62 %	58 %
21	100 %	91 %	88 %	61 %	61 %
23	100 %	84 %	87 %	79 %	74 %
25	100 %	81 %	81 %	–	71 %
Average		86 %	84 %	66 %	65 %

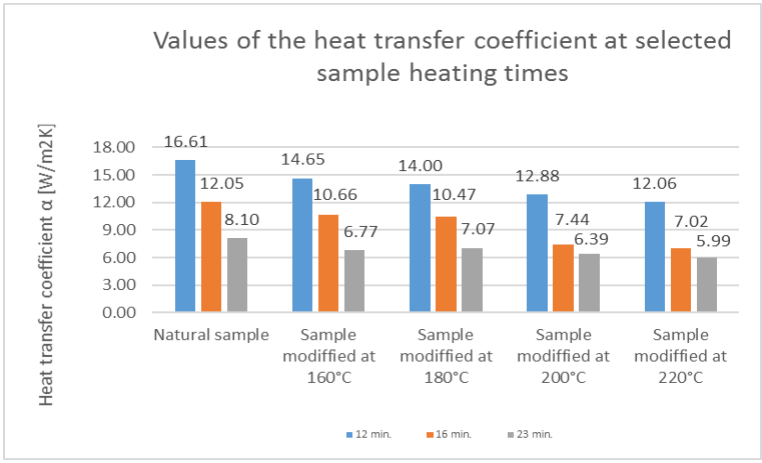

Fig. 6. Dependences of the heat transfer coefficient on the heating time of the samples
Obr. 6. Závislosti koeficientu prestupu tepla na čase ohrevu vzoriek

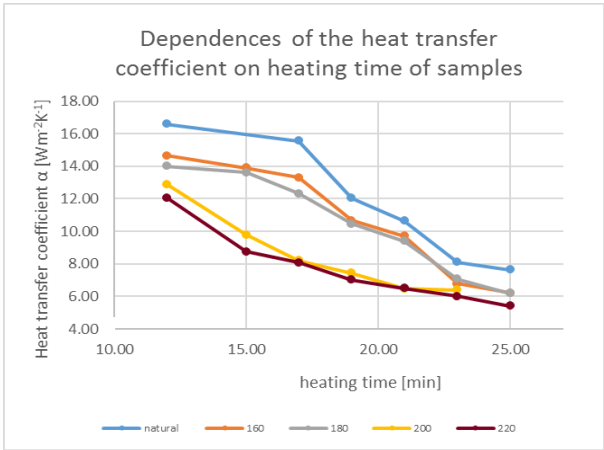

Fig. 7. Values of the heat transfer coefficient α at selected sample heating times
Obr. 7. Hodnoty koeficientu prestupu tepla α vo vybraných časoch ohrevu

DISCUSSION

In Fig. 7, it is visible that the value of the heat transfer coefficient α for all samples of thermally modified wood was lower than the value corresponding to the control sample. In the observed range, it is observable that the value of the heat transfer coefficient decreases with increasing degree of thermal modification. The difference between the control sample and the sample modified at 160 °C is, according to Table 2, a decrease in the range of 9–19 %. The largest difference was between the samples modified at 180 °C and 200 °C, which ranged from 6 to 26 %. Minor, but still observable differences were between samples treated at 160 °C and 180 °C in the range of 0–6 % and between samples treated at 200 °C and

220 °C in the range of 0–5%. The differences according to Table 1 had a smaller range at the end of the experiment (α = 7.64 – 5.42 $Wm^{-2}K^{-1}$) than at the beginning of the measurement (α = 16.61 – 12.06 $Wm^{-2}K^{-1}$). The largest difference was recorded in the 17th minute (α = 15.57 – 8.07 $Wm^{-2}K^{-1}$).

From the result, it can be concluded that the thermal modification has an effect on the heat transfer coefficient. The degree of wood treatment also has an effect – at higher temperatures of thermal modification, the heat transfer coefficient is significantly lower. With equation (8), the heat transfer coefficient can be considered as proportional to thermal conductivity of the sample.

This result is similar to findings of (Kol, Keshin, 2016), (Olarescu et al., 2015) and (Pásztory et al., 2017), who studied thermal conductivity of wood modified by Thermowood method. Mentioned works concluded that thermal modification decreases thermal conductivity of studied wood types.

As mentioned by (Kol, Keshin, 2016), Thermal conductivity of wood material is affected from wood species, moisture content, grain direction, direction of heat flow, density, extractives, defects and temperature. Process of heat treatment reduces both density (Tab. 1) and moisture content of the wood. This subsequently lowers both thermal conductivity and heat transfer coefficient of the modified wood.

The heat transfer coefficient α also decreased with gradual heating of the sample. This decrease could be due to the higher air temperature in the boundary layer. In the presence of heated air, the temperature difference in close proximity above the sample surface was lower than the temperature difference between the sample surface and the ambient air.

The method of holographic interferometry was used in the experiment, which allowed the visualization of the distribution of temperature fields over the heated sample. To be able to get useful data from the interferograms, it was necessary that they contain at least two interference fringes. This required a sufficient temperature difference between the sample and the ambient air. This condition was met at the 12th minute of sample heating. In cases where the interference fringes had shape that did not allow calculations, the closest suitable interferogram with the appropriate temperature values was used. In the control sample at 15 minutes, the heat transfer coefficient α could not be determined from the obtained interferograms. Therefore, this time is not included in Table 2.

In contrary to the hot and cold plate method used by (Kol, Keshin, 2016), (Olarescu et al., 2015) and (Pásztory et al., 2017), holographic interferometry was used for data evaluation. Result leads to similar conclusion: thermal modification influences the heat transfer coefficient. Also, degree of wood treatment has an effect – at higher temperatures of thermal modification, the heat transfer coefficient is significantly lower.

CONCLUSION

The experiment showed that thermal modification of wood reduces the intensity of heat transfer. *Compared* to the control sample, the thermally modified samples achieved lower final values in the whole measurement range. The heat transfer coefficient α decreased with increasing degree of thermal modification.

The *experiment* shows that thermal modification has a positive effect on wood when used as a barrier to heat loss. According to the average values in Table 3, the heat transfer coefficient was reduced by 14 %, at 180 °C by 16 %, at 200 °C by 34 % and at 220 °C by 35 % by thermal modification at 160 °C when compared to the control sample. This could

be due to reduction in moisture content and density of samples, which occurs as result of thermal modification.

According to Equation (1), when used in outdoor conditions, heat transfer will be additionally affected by atmospheric conditions such as humidity and air pressure, the presence and intensity of air flow. The heat transfer coefficient will depend on the temperature *difference* at the interface, so it will also be affected by the season and the alternation of days and nights.

Decrease of heat transfer coefficient occurred also among individual samples, over heating progress. The decrease ranged from $\alpha = 22.66$ $Wm^{-2}K^{-1}$ to $\alpha = 8.6$ $Wm^{-2}K^{-1}$ for control sample, from 21.26 $Wm^{-2}K^{-1}$ to 8.15 $Wm^{-2}K^{-1}$ for 160 °C sample, from 20.09 $Wm^{-2}K^{-1}$ to 7.36 $Wm^{-2}K^{-1}$ for 180 °C sample, from 14.84 $Wm^{-2}K^{-1}$ to 6.87 $Wm^{-2}K^{-1}$ for 200 °C sample and from 11.14 to 5.5 for 220 °C sample.

This could be caused by presence of boundary layer of heated air, which causes smaller temperature difference between object and ambient air.

When compared to studies on thermal conductivity of thermally modified natural fir and beech wood (Kol, Sefil, 2011), and spruce and poplar wood (Pásztory et al., 2017), similar result was achieved. In this study focused on heat transfer coefficient, results are dispersed in larger range. Difference could occur due to multiple factors, such as type of wood, moisture content or variation in time intervals of heat treatment. In further experimentation, more samples should be used for testing. Also, an experiment could be done, where holographic interferometry and hot and cold plate method would be used for examination of samples of same origin and treatment.

The holographic interferometry method seems to be an effective tool in heat transfer study. Visualization of temperature fields can be applied to a variety of materials, such as aerated concrete (Pivarčiová et al., 2019) or to test the functionality of heat exchange surfaces (Božek, 2014). Holographic interferograms using the Fourier-Mellin transform find application in automation processes by enabling the calculation of image shift and rotation (Božek, Pivarčiová, 2012).

ACKNOWLEDGMENT

This research was funded by VEGA 1/0086/18: Researching Temperature Fields in a Set of Shaped Heat Transfer Surfaces.

LITERATURE

SEBORG, R., MILLETT, M.A., STAMM, A. J. 1956. Heat-stabilized compressed wood (staypack): technical report. Madison, Wisconsin (USA): Department. of Agriculture, Forest Service, Forest Products Laboratory. Report no. 1580, 11 p. [online] [accessed October 2020] Available on: https://www.fpl.fs.fed.us/documnts/fplr/fplr1580.pdf

KOLLMANN, F., SCHNEIDER, A. 1963. Über das Sorptionsverhalten wärmebehandelter Hölzer. Holz Als Roh Und Werkstoff, vol. 21, pp. 77–85.

BURMESTER, A. 1973. Einfluß einer Wärme-Druck-Behandlung halbtrockenen Holzes auf seine Formbeständigkeit. Holz als Roh und Werkstoff, vol. 31, no. 6, pp. 237–243. Available on: https://doi.org/10.1007/BF02607268

GIEBELER, E. 1983. Dimensionsstabilisierung von Holz durch eine Feuchte/Wärme Druck-Behandlung. Holz als Roh und Werkstoff 1983, vol. 41, pp. 87–94. Available on: https://doi.org/10.1007/BF02608498

REINPRECHT, L., VIDHOLDOVÁ, Z. 2008. Mould resistance, water resistance and mechanical properties of OHT-thermowoods. In Sustainability through new technologies for enhanced wood durability, Proceedings of Socio-economic perspectives of treated wood for the common European market Final Conference, Bordeaux, France, 29–30 September 2008; Ghent University: Gent, Belgium, 2008; ISBN 9789080656505, pp. 159–156.

BOONSTRA, M. 2008. A two-stage thermal modification of wood. Thesis to obtain rank of Doctor. Université Henri Poincaré, France, Nancy 1, 29. 3. 2008. Available on: https://hal.univlorraine.fr/tel-01748345/document

NIEMZ, P., HOFFMAN, T., RÉTFALVI, T. 2010. Investigation of chemical changes in the structure of thermally modified wood. Maderas. Ciencia y tecnología, vol. 12, no. 2, pp. 67–78. Available on: http://dx.doi.org/10.4067/S0718221X2010000200002

KOL, S.H., KESHIN, S.A. 2016 The thermal conductivity of solid wood heat-treated using the thermowood method. Proceedings of Interational Conference on Material Science and Technology in Cappadoccia (IMSTEC'16). Nevsehir: Nevsehir Haci Bektas Veli University, Turkey, 6/8 April 2016; Kurt, B., Carboga, C., Öztürk, B., Z.; pp. 942–946. Available on: https://www.imstec.org/yazim_formatlari/IMSTEC›16%20PROCEEDINGS%202.revize.pdf

KOL, H.Ş., SEFIL, Y. 2011. The thermal conductivity of fir and beech wood heat treated at 170, 180, 190, 200, and 212°C. Applied Polymer Science, vol. 121, pp. 2473-2480. Available on: https://doi.org/10.1002/app.33885

KORKUT, D., HIZIROGLU, S., AYTIN, A. 2013. Effect of Heat Treatment on Surface Characteristics of Wild Cherry Wood. BioResources, vol. 8, no. 2, pp. 1582-1590.

OLARESCU CM., CAMPEAN M., COSEREANU C. 2015. Thermal conductivity of solid wood panels made from heat-treated spruce and lime wood strips. PRO Ligno, vol. 11, no. 4, pp. 377–382

PÁSZTORY, Z., HORVÁTH, N., BÖRCSÖK, Z. 2017. Effect of heat treatment duration on the thermal conductivity of spruce and poplar wood. European Journal of Wood and Wood Products, vol. 75, pp. 843–845. Available on: https://doi.org/10.1007/s00107-017-1170-2

CZAJKOWSKI, Ł., OLEK, W., WERES, J. 2020. Effects of heat treatment on thermal properties of European beech wood. European Journal of Wood and Wood Products, vol. 78, pp. 425–431. Available on: https://doi.org/10.1007/s00107-020-01525-w

International Thermowood Association. 2003 ThermoWood Handbook. Unioninkatu, Helsinky, Finland, 2003; 66 p. Available on: https://asiakas.kotisivukone.com/files/en.thermowood.palvelee.fi/downloads/tw_handbook_080813.pdf

BARCÍK, Š., GAŠPARÍK, M. 2014. Effect of Tool and Milling Parameters on the Size Distribution of Splinters of Planed Native and Thermally Modified Beech Wood. BioResources, vol. 9, no. 1, pp. 1346 – 1360. [cit. 2020–10–01]. Available on: https://ojs.cnr.ncsu.edu/index.php/BioRes/article/view/4990

KOL, H.Ş., SEFIL, I., AYSAL, S. 2015. Effect of heat treatment on the mechanical properties, and dimensional stability of fir wood. Proceedings of the 27th International Conference Research for Furniture Industry, Ankara, Turkey, 17–18 September 2015; pp. 269–279. Available on: http://www.furnituredesign2015.org/assets/icrfi_tr_138.pdf

KUBS, J., GAŠPARÍK, M., GAFF, M., KAPLAN, L., ČEKOVSKÁ, H., JEŽEK, J., ŠTÍCHA, V. 2017. Influence of Thermal Treatment on Power Consumption during Plain Milling of Lodgepole Pine (Pinus contorta subsp. murrayana) BioResources, vol. 12, no. 1, pp. 407–418. Available on: DOI: 10.15376/biores.12.1.407-418

KOLEDA, P., KORČOK, M., BARCÍK, Š., IĽAŠ, Š. 2018. Effect of temperature of heat treatment on energetic intensity of flat milling of picea abies. Management Systems in Production Engineering, vol. 26, pp. 151 – 156. Available on: https://doi.org/10.1515/mspe-2018-0024 Available on: https://doi.org/10.1007/BF02609705

KORČOK, M.; KOLEDA, P.; BARCÍK, Š.; VANČO, M. Effect of technical and technological parameters on the surface quality when milling thermally modified European oak wood. Management Systems in Production Engineering 2018, vol. 26, no. 3, pp. 151–156. Available on: https://doi.org/10.1515/mspe-2018-0024

CUI, X., MATSUMURA, J. 2019. Wood Surface Changes of Heat-Treated Cunninghamia Inaceolate Following Natural Weathering. Forests, vol. 10, no. 9, p. 791. Available on: https://doi.org/10.3390/f10090791

KAČÍKOVÁ, D., KUBOVSKÝ, I., ULBRIKOVÁ, N., KAČÍK, F. 2020. The Impact of Thermal Treatment on Structural Changes of Teak and Iroko Wood Lignins. Applied Sciences, vol. 10, no. 14, p. 5021. Available on: https://doi.org/10.3390/app10145021

KMINIAK, R., ORLOWSKI, K.A., DZURENDA, L., CHUCHALA, D., BANSKI, A. 2020. Effect of Thermal Treatment of Birch Wood by Saturated Water Vapor on Granulometric Composition of Chips from Sawing and Milling Processes from the Point of View of Its Processing to Composites. Applied Sciences, vol. 10, no. 21, p. 7545. Available on: https://doi.org/10.3390/app10217545

PIVARČIOVÁ, E. 2002. Possibilities of visualization and analysis of temperature fields at thermic degradation of wood. Dissertation thesis, Technická univerzita vo Zvolene, Zvolen, 2002

PIVARČIOVÁ E., BARCÍK Š., ŠTEFKOVÁ J., ŠKULTÉTY E. 2019. Investigation of Temperature Fields in the Air Environment above Wood Subjected to Thermal Degradation. Drvna Industrija, vol. 70, no. 4, pp. 319-327 Available on: https://hrcak.srce.hr/index.php?show=clanak&id_clanak_jezik=334009

HRČKOVÁ, M., KOLEDA, P., KOLEDA, P., BARCÍK, Š., ŠTEFKOVÁ, J. 2018. Color Change of Selected Wood Spieces Affected by Thermal Treatment and Sanding. BioResources, vol. 13, no. 4, pp. 8956–8975. Available on: https://bioresources.cnr.ncsu.edu/resources/color-change-of-selected-wood-species-affected-by-thermal-treatment-and-sanding/

PIVARČIOVÁ, E., BOŽEK, P., DOMNINA, K., ŠKULTÉTY, E., FEDOSOV, S. 2019. Interferometric measurement of heat transfer above new generation foam concrete. Measurement Science Review, vol. 19, no. 4, pp. 153–160. Available on: https://doi.org/10.2478/msr-2019-0021

ČERNECKÝ, J., PIVARČIOVÁ, E. 2011. Vizualizační a optické měřicí metody. Available online: https://eu.fme.vutbr.cz/file/vomm/index.htm (Accessed on 10. 1. 2021)

ČERNECKÝ, J., KONIAR, J., BRODNIANSKA, Z. 2012. Optimalizácia výmenníkov tepla s využitím experimentálnych metód a fyzikálneho modelovania. Technická univerzita vo Zvolene: Zvolen, Slovak republic 2012. ISBN 978-80-228-2325-8.

KOSSACZKÝ, E., SUROVÝ, J. 1963. Chemické inžinierstvo I, 3rd ed.; Slovenské vydavateľstvo technickej a ekonomickel literatúry: Bratislava, Slovak republic, 1963; pp. 250–252.

BRODNIANSKA, Z. 2019. Experimental investigation of convective heat transfer between corrugated heated surfaces of rectangular channel. Heat Mass Transfer 2019, vol. 55, pp. 3151–3164. Available on: https://doi.org/10.1007/s00231-019-02649-3

BOŽEK, P. 2014. Automated Detection Type Body and Shape Deformation for Robotic Welding Line. In: Advances in Systems Science, Volume 240, pp. 229–240. Available on: https://doi.org/10.1007/978-3-319-01857-7_22

BOŽEK, P., PIVARČIOVÁ, E. 2012. Registration of Holographic Images Based on Integral Transformation. Computing and Informatics 2012, vol. 31, no. 6, pp. 1369–1383. Available on: http://www.cai.sk/ojs/index.php/cai/article/view/772/0

Corresponding author:
Áron Hortobágyi, tel.: +421917394179, e-mail: xhortobagyi@is.tuzvo.sk